J Mater Sci (2013) 48:377–412
DOI 10.1007/s10853-012-6755-x

Experimental study and thermodynamic modelling of the ternary Al–Fe–Ta system

V. T. Witusiewicz · A. A. Bondar · U. Hecht · V. M. Voblikov · N. I. Tsyganenko · O. S. Fomichov · M. V. Karpets · V. M. Petyukh · T. Y. Velikanova

Received: 27 April 2012 / Accepted: 19 July 2012 / Published online: 14 August 2012

Abstract In the present article, a thermodynamic description of the ternary Al–Fe–Ta system is proposed, being obtained by CALPHAD modelling based on assessed experimental information from literature and our own experimental results. Dedicated experiments were performed to complement literature data on phase equilibria and thermodynamic properties. As-cast and annealed samples were prepared and analysed by means of SEM/EDS, XRD, DTA and DSC techniques, as well as isoperibolic dissolution calorimetry. The experiments revealed that three binary phases have large ternary extensions: the C14 Laves phase based on $TaFe_2$ dissolves up to about 56 at.% Al, the μ or $D8_5$ phase dissolves up to about 39 at.% Al and the σ phase based on Ta_2Al dissolves up to 12 at.% Fe. The ternary ordered Heusler phase $L2_1$ (the $MnCu_2Al$ crystal structure type) is modelled as a stable phase such that it forms through a second-order ordering process at 1122 K from the ordered B2 phase of composition $Ta_{0.04}Fe_{0.50}Al_{0.46}$ involving the substitution of Al with Ta atoms and reaches $TaFe_2Al$ stoichiometry at ambient temperatures. The elaborated thermodynamic description was applied to calculate selected phase equilibria as to provide a comparison between calculated and experimental results. The calculations are shown to reproduce reasonably the experimental data.

Electronic supplementary material The online version of this article (doi:10.1007/s10853-012-6755-x) contains supplementary material, which is available to authorized users.

V. T. Witusiewicz (✉) · U. Hecht
ACCESS e.V, Intzestr. 5, 52072 Aachen, Germany
e-mail: v.vitusevych@access-technology.de

A. A. Bondar · V. M. Voblikov · N. I. Tsyganenko · O. S. Fomichov · M. V. Karpets · V. M. Petyukh · T. Y. Velikanova
Frantsevich Institute for Problems of Materials Science, Krzhyzhanovsky Str. 3, 03680 Kyiv, Ukraine

Introduction

The Al–Fe–Ta system is of interest for iron aluminides reinforced with the Laves phase λ-($TaFe_2$) and/or Heusler phase ($L2_1$) [1–5], as well as for eutectic (Fe) + λ [6] and various magnetic alloys. Ordered Al–Fe–Ta alloys strengthened by λ show good creep behaviour, high strength and good corrosion resistance at elevated temperatures [2, 4, 7–9]. They can be prepared by ingot metallurgy and are attractive materials since the mechanical properties can be optimised through adjustment of the Ta content, which controls the volume fraction of the Laves phase, and adjustment of the Al content, which controls the atomic order in the Fe–Al matrix [7]. A consistent thermodynamic description of the ternary system is required for microstructure optimization of such materials [5]. The description proposed 20 years ago [10] is inconsistent with latest research results.

The study reported here aimed to construct the phase diagram for a wide temperature range and to provide an improved thermodynamic description of the entire Al–Fe–Ta system. Published data on phase equilibria and thermodynamic properties for this system were analysed and complemented by our own experimental results. The assessed literature data, experimental results obtained in the present work and recently published descriptions of the constituent binary systems Al–Fe [11], Al–Ta [12] and Fe–Ta [13] were used for CALPHAD modelling (Computer Coupling of Phase Diagrams and Thermochemistry).

The article is structured as follows: in the second and third section, the experimental data are presented with

main emphasis on the measurements performed within the frame of this study. The forth section contains a brief description of the thermodynamic models used for expressing the Gibbs free energy of the individual phases of the alloy system and a description of the optimization procedure. The resulting thermodynamic database is given in Appendix. In the fifth section, a large number of calculations performed with the elaborated thermodynamic description, including the complete Scheil's reaction scheme, liquidus and solidus projections, isothermal sections and selected isopleths. The calculations are discussed in comparison with experimental data regarding phase equilibria of major interest.

Literature data for the ternary Al–Fe–Ta system

The Al–Fe–Ta system was recently assessed by Ghosh [14], who substantially enhanced previous reviews [15–17]. Table 1 summarizes the crystallographic data for all known phases of the system, taken from [11–14]. As shown in [14], the main composition range studied so far was limited to the Al- and Ta-lean region with less than 35 at.% Al and 50 at.% Ta, respectively. Besides this region, experimental investigations were reported in [18, 19] for the rapidly solidified $Ta_{10}Fe_{20}Al_{70}$ alloy that formed the metastable icosahedral *i*-phase with the quasilattice constant of $a = 460.0 \pm 0.3$ pm. Heating at 10 K min^{-1} gave rise to decomposition of the *i*-phase into Fe_4Al_{13} and $TaAl_3$ (ε) at about 900 K [18].

The partial isothermal section at $T = 1273$ K was investigated experimentally by Hunt and Raman [20], Risanti and Sauthoff [7] and further modified by Ghosh [14]. At this temperature, the phases λ and μ present in the binary constituent system Fe–Ta display extensive solubility for Al replacing Fe. Interestingly, above references indicate a termination of the two single-phase fields λ and μ at a characteristic Al content, both phases re-appearing as λ' and μ', once the Al content increases further. However, in recent publications [23, 24], Risanti and Sauthoff attributed this to impurity effects and proposed that the single Laves phase field extends to 50 at.% Al without interruption.

Other data on two-phase equilibria between (Fe) and λ were reported by Reviere et al. [6] and Von Keitz et al. [21] obtained from the as-cast samples, Risanti and Sauthoff at 1473 and 1073 K [3, 7, 22–24], as well as Palm et al. [9] at 1073 and 873 K. For single Laves phase samples, the reported differential thermal analyses (DTA) showed that the addition of Al led to a slight reduction of melting temperature and X-ray diffraction (XRD) measurements revealed an increase of the lattice parameters [21].

Anthony and Fultz [25] experimentally investigated the effect of Ta on the critical temperature of the $D0_3$–B2 transformation in four alloys ($Fe_{74}Al_{26}$, $Ta_1Fe_{73}Al_{26}$, $Ta_2Fe_{72}Al_{26}$ and $Ta_4Fe_{70}Al_{26}$) by XRD and DTA. They reported an increase of the transformation temperature from 823 K for the binary sample to 858 K with addition of 1 at.% Ta, above which it remains at the same level due to the limited solubility of Ta in $D0_3$. Consequently, the authors [25] pointed out the solubility limit of Ta in $D0_3$ to be less 1 at.%. Unlike in [7, 22], the latest publications of Risanti and Sauthoff [23, 24] confirmed the above trend: the transformation temperature reaches 873 K for an alloy $Ta_2Fe_{73}Al_{25}$ and decreases to 853 K with further increasing the Ta content to 6 at.% (the Al content is constant). The latest papers [2, 9, 24] indicated that at 923 K fine coherent $L2_1$ particles precipitated in the alloy $Ta_2Fe_{73}Al_{25}$ under creep load applied for 600 h. In this temperature domain, phase equilibria for alloys along the section Fe_3Al–Ta (0 to 6 at.% Ta) are quite complex and require further investigation. Already in the constituent binary Al–Fe system [11] (see also Fig. 11a of the present study) order–disorder transformations in the vicinity of the Fe_3Al composition are sensitively depending on the Al content: in cooling the alloy $Fe_{74}Al_{26}$, the sequence of ordering transformations is B2\$D0_3$ (second-order at $T = 853$ K) followed by $D0_3$\ $D0_3 + A2^{fm}$[1] (first-order at $T = 818$ K), while alloy $Fe_{75}Al_{25}$ gives another transformation sequence, i.e. B2\$A2^{fm} + B2$ (first-order at $T = 854$ K) and $A2^{fm} + B2$\$A2^{fm} + D0_3$ (a second-order invariant reaction $B2 \leftrightarrows A2^{fm} + DO_3$ at $T = 839$ K).

So far, no experimental data regarding thermodynamic properties of ternary Al–Fe–Ta alloys were reported in literature. Bozzolo et al. [26] calculated the formation energy of B2 ternary alloys $Ta_xFe_{50-x}Al_{50}$ and $Ta_xFe_{50}Al_{50-x}$ ($x = 0,\ldots, 1.39$) by the Bozzolo–Ferrante–Smith muffin-tin orbital method. For the latter alloys, the partial ordering energy was also calculated by Mekhrabov and Akdeniz [27] applying the quasi-chemical method combined with electronic theory in the pseudo-potential approximation.

Additional experiments

Preparation of samples

Aiming to examine phase equilibria in the Al–Fe–Ta system, in total, 19 alloys were prepared by arc melting with a non-consumable tungsten electrode on a water-cooled copper hearth under purified argon. The samples, with a mass of

[1] The A2, B2, $D0_3$ and $L2_1$ phases in para- and ferromagnetic states are treated as different phases due to dissimilar point group symmetry. To distinguish between the different states, the ferromagnetic state is marked with superscript 'fm' throughout the article. The back slash '\' denotes crossing of a phase boundary.

Table 1 Phase designations most often used in literature for the Al–Fe–Ta system along with crystal structure data [11–14] and thermodynamic models used in the present description

Phase (designation)	Pearson symbol	Space group	Strukturbericht designation	Prototype	Sublattice model used in the present description
A1[a], (Al), (αAl), (γFe), fcc_A1	*cF4*	*Fm*$\bar{3}$*m*	A1	Cu	{[(Al, Fe, Ta)$_1$: (Va)$_1$] + [(A , Fe, Ta)$_{0.25}$: (Al, Fe, Ta) $_{0.25}$: (Al, Fe, Ta)$_{0.25}$: (Al, Fe, Ta)$_{0.25}$: (Va)$_1$]}
L1$_0$, fcc_L1$_0$	*tP2*	*P4/mmm*	L1$_0$	CuAu	
L1$_2$, fcc_L1$_2$	*cP4*	*Pm*$\bar{3}$*m*	L1$_2$	Cu_3Au	
A2, β, (Ta), (αFe), (δFe), bcc_A2	*cI2*	Im$\bar{3}$*m*	A2	W	{[(Al, Fe, Ta)$_1$: (Va)$_3$] + [(Al, Fe, Ta)$_{0.25}$: (Al, Fe, Ta) $_{0.25}$: (Al, Fe, Ta)$_{0.25}$: (Al, Fe, Ta)$_{0.25}$: (Va)$_3$]}
B2, β_0, β', bcc_B2, FeAl	*cP2*	*Pm*$\bar{3}$*m*	B2	CsCl	
D0$_3$, Fe_3Al	*cF16*	*Fm*$\bar{3}$*m*	D0$_3$	BiF_3	
L2$_1$, $TaFe_2Al$, Heusler phase	*cF16*	*Fm*$\bar{3}$*m*	L2$_1$	$MnCu_2Al$	
Fe_5Al_8	*cI52*	*I*$\bar{4}$3*m*	D8$_2$	Cu_5Zn_8	[(Al, Fe, Ta) $_8$: (Al, Fe, Ta) $_5$]
$FeAl_2$	*aP18*	*P1*	–	Fe Al_2	[(Al, Ta)$_2$: (Fe)$_1$]
Fe_2Al_5	*oC?*	*Cmcm*	–	–	[(Al, Ta)$_5$: (Fe)$_2$]
Fe_4Al_{13}, $FeAl_3$	*mC102*	*C2/m*	–	–	[(Al)$_{0.6275}$: (Fe)$_{0.2350}$: (Al, Fe, Ta)$_{0.1375}$]
ε, $TaAl_3$	*tI8*	*I4/mmm*	D0$_{22}$	$TiAl_3$(h)	[(Al)$_{0.75}$: (Al, Fe, Ta)$_{0.25}$]
κ, δ, $Ta_{39}Al_{69}$	*cF432*	*F*$\bar{4}$3*m*	–	$Ta_{39}Al_{69}$	[(Al, Fe, Ta)$_{0.6389}$: (Al, Fe, Ta)$_{0.3611}$]
φ, $Ta_{48}Al_{38}$,TaAl	*mP86*	*P2$_1$/c*	–	$Ta_{48}Al_{38}$	[(Al, Fe, Ta)$_{0.8837}$: (Al, Fe, Ta)$_{1.1163}$]
σ, Ta_2Al	*tP30*	*P42/mmm*	D8$_b$	σCrFe	[(Al, Fe, Ta)$_{0.533}$: (Al, Fe, Ta)$_{0.333}$: (Ta)$_{0.134}$]
λ, ε, $TaFe_2$, C14, Laves phase	*hP12*	*P6$_3$/mmc*	–	$MgZn_2$	[(Al, Fe, Ta)$_2$: (Al, Fe, Ta)$_1$]
μ, TaFe, Ta_6Fe_7	hR39	*R*$\bar{3}$*m*	–	W_6Fe_7	[(Al, Fe, Ta)$_7$: (Ta)$_2$: (Al, Fe, Ta)$_4$]
Ta_3Fe_2 (metastable)	–	–	–	–	[(Al, Fe, Ta)$_2$: (Al, Fe, Ta)$_3$]
i-phase (metastable)	Icosahedral quasicrystal phase				–

[a] Designations given in *bold letters* are used throughout the present study

15 g each, solidified at a cooling rate of about 100 K s^{-1}. The initial materials were bulk Al (purity 99.999 wt%, Kirov's Plant, Volkhov, Russia), bulk Ta (purity 99.97 wt%, Ulbinskiy Metallurgical Plant, Russia) and carbonyl iron (purity 99.95 wt%, P/B 4019, Russia), as well as master-alloys (at.%) $Ta_{43.4}Al_{56.6}$, $Ta_{25.2}Al_{74.8}$ and $Ta_{51.3}Fe_{48.7}$. The master alloys were prepared using above-mentioned pure elements and the same preparation procedure.

The sample compositions are listed in Table 2 and pertain to four groups: (i) samples located in vicinity of 13 at.% Ta (samples no. 1–10); (ii) samples consisting of mainly Laves phase and containing about 32 at.% Ta (samples no. 11–14); (iii) samples consisting of mainly μ phase and containing about 52 at.% Ta (samples no. 16–18); and (iv) samples with about 13 at.% Fe (samples no. 5, 11, 15, 16 and 19). An alloy with composition $Ta_{2.0}Fe_{73.5}Al_{24.3}C_{0.2}$ (sample no. 20) received from Max-Planck-Institut für Eisenforschung GmbH (Düsseldorf, Germany) for casting trials was also investigated. Moreover, this material was unidirectionally solidified in a Bridgman furnace [28] and quenched after planar growth and dendritic growth. This allowed to evaluate equilibrium and non-equilibrium compositions of the bcc A2(B2) and liquid phases.

As measured by reducing extraction in a Ni bath followed by chromatography, the oxygen content in the samples ranged from 0.03 to 0.07 wt% and the contamination by N and H was lower than the detection limit (about 0.001 wt% N and 0.003 wt% H). Carbon contamination was determined to range from 0.02 to 0.04 wt%, originating mainly from the Fe and Ta used. The samples were chemically analysed and studied in the as-cast state as well as after annealing at selected temperatures (see Table 2) by means of scanning electron microscopy (SEM), energy dispersive X-ray analysis (EDS), XRD, DTA, differential scanning calorimetry (DSC) and isoperibolic dissolution calorimetry.

Annealing treatments of all samples were performed at a defined temperature close to the alloy's solidus (40–70 K below T_{sol}) for 5–8 h in a resistance furnace with a tungsten heater in argon atmosphere gettered by Ti, Zr or Hf cuttings. This annealing treatment is called 'subsolidus annealing' further on. The cooling rate after annealing ranged around 3 K s^{-1}. Several selected samples were further annealed at 1123 K for 744 h, at 923 K for 482 h and at 823 K for 362 h in a tube furnace. The samples were sealed under Ar in quartz ampoules and quenched in water after completed annealing.

SEM/EDS analysis of samples

SEM/EDS were carried out in a ZEISS-LEO-type Gemini 1550 microscope (Karl Zeiss, Inc., Germany) equipped with an energy dispersive X-ray analysis system (INCA

Table 2 Alloy compositions, XRD data on phase constituents, lattice parameters and SEM/EDS data for the composition of coexisting phases in as-cast and annealed Al–Fe–Ta samples

Sample no.	EDS composition, at.%		State of sample	Phase constituent[a]/ structure constituent	Lattice parameters[b], pm or (°)	Composition of phases, at.%	
	Ta	Fe				Ta	Fe
1	13.4 ± 0.3	51.2 ± 0.1	as-cast	**λ**	$a = 490.7$; $c = 798.5$	29.9 ± 0.6	44.1 ± 0.6
				A2	$a = 292.0$	4.3 ± 0.1	54.6 ± 0.3
			1553 K/5 h	λ	$a = 491.1$; $c = 798.8$	29.1 ± 0.2	42.8 ± 0.4
				A2	$a = 292.0$	4.7 ± 0.1	55.5 ± 0.3
			1553 K/5 h + 1123 K/ 744 h	λ	$a = 490.5$; $c = 797.0$	28.8 ± 1.1	45.1 ± 1.0
				B2	$a = 293.0$	7.7 ± 1.4	51.8 ± 0.4
			1553 K/5 h + 923 K/ 482 h	λ	$a = 490.6$; $c = 798.6$	28.2 ± 0.4	45.8 ± 0.2
				B2	$a = 292.0$	3.6 ± 0.2	53.7 ± 0.2
				$L2_1$	$a \approx 583$	[d]	
2	13.5 ± 0.2	62.6 ± 0.5	as-cast	**λ**	$a = 486.4$; $c = 792.0$	28.3 ± 0.4	54.8 ± 0.4
				A2	$a \approx 292$	2.7 ± 0.1	66.7 ± 0.4
			1623 K/5 h	λ	$a = 486.4$; $c = 791.6$	27.2 ± 0.4	54.3 ± 0.6
				A2	$a \approx 292$	2.6 ± 0.1	67.5 ± 0.2
			1623 K/5 h + 1123 K/ 744 h	λ	$a = 486.4$; $c = 791.9$	27.9 ± 0.1	55.5 ± 0.1
				B2	$a = 292.2$	2.8 ± 0.1	64.7 ± 0.1
			1623 K/5 h + 923 K/ 482 h	λ	$a = 486.5$; $c = 791.8$	28.4 ± 0.5	55.2 ± 0.5
				B2	$a = 291.9$	2.5 ± 0.1	65.2 ± 0.4
3	13.3 ± 0.2	72.0 ± 0.3	as-cast	**λ**	$a = 483.3$; $c = 788.0$	27.7 ± 0.4	63.0 ± 0.5
				A2	[c]	0.9 ± 0.2	78.3 ± 0.4
				eutectic	–	6.2 ± 0.2	75.8 ± 0.2
			1673 K/5 h	λ	$a = 482.9$; $c = 787.0$	26.5 ± 0.3	63.3 ± 0.4
				A2	$a = 290.4$	0.7 ± 0.2	78.7 ± 0.3
			1673 K/5 h + 1123 K/ 744 h	λ	$a = 484.2$; $c = 789.1$	27.9 ± 0.5	62.6 ± 0.4
				A2	$a = 291.1$	0.3 ± 0.1	76.1 ± 0.3
			1673 K/5 h + 923 K/ 482 h	λ	$a = 483.3$; $c = 778.5$	27.3 ± 0.4	63.7 ± 0.4
				A2	$a = 290.8$	1.0 ± 0.1	76.2 ± 0.3
4	12.8 ± 0.25	80.4 ± 0.3	as-cast	**λ**	$a = 481.8$; $c = 785.0$	28.1 ± 0.3	68.0 ± 0.4
				A2	$a \approx 289$	0.7 ± 0.2	89.4 ± 0.1
				eutectic	–	6.5 ± 0.3	85.5 ± 0.3
			1673 K/5 h	λ	$a = 480.8$; $c = 784.7$	26.7 ± 0.2	69.6 ± 0.6
				A2	$a = 289.2$	0.8 ± 0.7	89.3 ± 0.4
5	12.8 ± 0.6	13.5 ± 0.8	as-cast	**λ**	$a = 501.9$; $c = 820.0$	33.7 ± 0.6	14.5 ± 0.5
				ε	$a = 384.2$; $c = 854.1$	25.5 ± 1.3	2.3 ± 1.1
				Fe_4Al_{13}	$a = 1549$; $b = 808$; $c = 1248$; $\beta = 107.2°$	0.4 ± 0.1	23.5 ± 0.3
			1343 K/8 h	λ	$a = 501.7$; $c = 820$	32.6 ± 0.2	16.7 ± 0.5
				ε	$a = 384.3$; $c = 854.7$	23.5 ± 0.2	1.6 ± 0.2
				Fe_4Al_{13}	$a = 1549$; $b = 808$; $c = 1248$; $\beta = 107.2°$	0.7 ± 0.1	23.2 ± 0.3
6	13.0 ± 0.4	21.3 ± 0.4	as-cast	**λ**	$a = 501.0$; $c = 816.3$	32.9 ± 0.5	19.2 ± 0.5
				ε	$a = 384$; $c = 855$	23.8 ± 1.6	2.8 ± 1.2
				Fe_4Al_{13}	[c]	0.7 ± 0.1	23.7 ± 0.6
			1343 K/8 h	λ	$a = 501.5$; $c = 819.5$	31.9 ± 0.6	17.7 ± 0.6
				ε	$a \approx 384$; $c \approx 855$	23.8 ± 0.2	1.6 ± 0.4
				Fe_4Al_{13}	$a = 1549$; $b = 806$; $c = 1248$; $\beta = 107.7°$	0.7 ± 0.1	23.3 ± 0.4
			1343 K/8 h + 1123 K/ 744 h	λ	–	31.9 ± 0.1	19.3 ± 0.7
				ε	–	22.1 ± 0.6	2.8 ± 0.8
				Fe_4Al_{13}	–	0.6 ± 0.1	23.6 ± 0.1

Table 2 continued

Sample no.	EDS composition, at.%		State of sample	Phase constituent[a]/ structure constituent	Lattice parameters[b], pm or (°)	Composition of phases, at.%	
	Ta	Fe				Ta	Fe
7	12.8 ± 0.4	28.1 ± 0.3	as-cast	**λ**	$a = 499.6$; $c = 813.1$	31.3 ± 0.2	25.0 ± 1.1
				Fe_2Al_5	$a \approx 766$; $b \approx 642$; $c \approx 421$	0.2 ± 0.1	28.5 ± 0.2
				eutectic	–	3.6 ± 1.0	28.2 ± 0.3
			1323 K/7 h	λ	$a = 499.8$; $c = 813.3$	31.7 ± 0.4	24.1 ± 0.4
				Fe_2Al_5	[c]	0.1 ± 0.1	29.0 ± 0.2
8	12.3 ± 0.3	30.0 ± 0.4	as-cast	**λ**	$a = 498.9$; $c = 811.4$	33.0 ± 0.1	25.1 ± 0.2
				Fe Al_2	[c]	0.6 ± 0.2	34.7 ± 3.0
				eutectic	–	3.3 ± 0.9	31.4 ± 0.6
			1343 K/8 h	λ	$a = 499.5$; $c = 812.0$	31.9 ± 0.4	25.3 ± 0.4
				Fe Al_2	[c]	0.2 ± 0.1	31.9 ± 0.5
			1123 K/744 h	λ	$a = 499.2$; $c = 811.6$	31.3 ± 0.1	26.2 ± 0.2
				$FeAl_2$	$a = 487.8$; $b = 647.0$; $c = 849.4$; $\alpha = 91.75°$; $\beta = 73.27°$; $\gamma = 96.89°$	0.03 ± 0.02	32.8 ± 0.2
9	12.7 ± 0.4	32.2 ± 0.1	as-cast	**λ**	$a = 498.4$; $c = 810.6$	31.7 ± 0.4	27.1 ± 0.2
				Al_2Fe	[c]	0.4 ± 0.1	32.9 ± 0.2
				B2[e]	$a \approx 292$ [c,e]	1.9 ± 0.4	43.4 ± 0.5
				eutectic	–	4.3 ± 0.2	31.6 ± 0.7
			1323 K/7 h	λ	$a = 498.4$; $c = 810.8$	31.5 ± 0.1	26.9 ± 0.5
				$FeAl_2$	[c]	0.2 ± 0.1	33.7 ± 0.3
10	13.2 ± 0.5	36.1 ± 0.5	as-cast	**λ**	$a = 497.0$; $c = 807.8$	30.7 ± 0.2	31.1 ± 0.3
				B2[e]	$a \approx 292$[c,e]	1.2 ± 0.1	45.0 ± 0.7
				$FeAl_2$	[c]	0.4 ± 0.1	34.5 ± 1.4
				eutectic	–	0.8 ± 0.1	37.9 ± 0.4
			1323 K/7 h	λ	$a = 497.8$; $c = 809.0$	30.6 ± 0.4	29.9 ± 0.9
				B2[e]	[c,e]	1.1 ± 0.1	47.6 ± 0.2
				$FeAl_2$	[c]	0.1 ± 0.1	33.4 ± 0.2
11	32.1 ± 0.4	13.2 ± 0.4	as-cast	**λ**	$a = 502.2$; $c = 821.4$	32.6 ± 0.2	15.3 ± 0.2
				ε	$a = 384.0$; $c = 853.6$	24.4 ± 0.1	0.9 ± 0.2
				Fe_4Al_{13}[f]	[c]	2.4 ± 1.0	22.0 ± 0.9
			1723 K/6 h	λ	$a = 502.1$; $c = 821.4$	32.5 ± 0.4	15.2 ± 0.4
				ε	$a = 384.0$; $c = 855.2$	24.5 ± 0.3	1.0 ± 0.2
				Fe_4Al_{13}[f]	[c]	2.3 ± 0.4	21.9 ± 0.6
12	31.7 ± 1.4	33.0 ± 0.7	as-cast	**λ**	$a = 496.2$; $c = 806.9$	35.3 ± 0.3	32.2 ± 0.4
				μ	[c]	[d]	
			1973 K/5 h	λ	$a = 495.2$; $c = 805.4$	32.6 ± 0.5	32.7 ± 0.3
				μ	[c]	49.7 ± 0.4	19.2 ± 0.5
13	31.6 ± 0.6	44.9 ± 0.5	as-cast	**λ**	$a = 491.4$; $c = 800.0$	34.0 ± 0.8	42.8 ± 0.2
				μ[f]	[c]	51.2 ± 0.2	28.0 ± 0.1
			1973 K/5 h	λ	$a = 490.9$; $c = 799.3$	32.0 ± 0.8	43.8 ± 0.4
				μ[f]	[c]	50.0 ± 0.4	27.5 ± 0.7
14	31.8 ± 0.5	53.1 ± 0.7	as-cast	**λ**	$a = 487.8$; $c = 795.1$	29.9 ± 2.6	54.9 ± 1.0
				μ[f]	[c]	50.9 ± 0.7	36.0 ± 0.7
			1973 K/5 h	λ	$a = 487.4$; $c = 794.3$	31.2 ± 0.5	53.7 ± 0.5
				μ[f]	[c]	50.3 ± 0.4	35.2 ± 0.6
15	37.4 ± 0.2	14.8 ± 1.2	as-cast	**λ**	$a = 502.2$; $c = 822.1$	34.3 ± 0.2	17.6 ± 0.3
				σ	$a = 981.6$; $c = 522.1$	56.4 ± 0.7	2.3 ± 0.2
				μ	[c]	50.8 ± 0.4	5.6 ± 0.2
			1823 K/6 h	λ	$a = 501.8$; $c = 821.1$	33.7 ± 0.5	16.1 ± 0.6
				σ	$a = 984.7$; $c = 520.6$	58.6 ± 0.5	1.8 ± 0.5
				μ	[c]	49.5 ± 0.2	11.9 ± 0.2

Table 2 continued

Sample no.	EDS composition, at.%		State of sample	Phase constituent[a]/ structure constituent	Lattice parameters[b], pm or (°)	Composition of phases, at.%	
	Ta	Fe				Ta	Fe
16	54.1 ± 0.4	12.1 ± 0.2	as-cast	***σ***	$a = 985.8$; $c = 517.2$	68.8 ± 0.3	6.2 ± 0.8
				μ	$a = 503.0$; $c = 2747$	48.1 ± 0.6	16.0 ± 0.8
				λ^f	$a \approx 491$; $c \approx 797$	[d]	
			1973 K/5 h	σ	$a = 986.4$; $c = 517.8$	68.6 ± 0.5	4.7 ± 0.2
				μ	$a = 503.1$; $c = 2747$	48.8 ± 0.5	15.8 ± 0.3
				λ^f	$a \approx 491$; $c \approx 797$	[d]	
17	53.3 ± 1.2	23.1 ± 0.5	as-cast	***μ***	$a = 501.9$; $c = 2748$	52.9 ± 0.8	25.9 ± 0.9
				σ	$a = 987.0$; $c = 518.5$	71.6 ± 0.4	11.3 ± 0.5
				λ^f	[c]	[d]	
			1973 K/5 h	μ	$a = 501.4$; $c = 2744$	51.9 ± 0.6	24.6 ± 0.6
				σ	$a = 988.0$; $c = 518.5$	74.0 ± 0.7	9.8 ± 0.8
				λ^f	[c]	[d]	
18	52.6 ± 0.5	32.8 ± 0.9	as-cast	***μ***	$a = 498.7$; $c = 2731$	52.7 ± 0.6	32.4 ± 0.7
			1973 K/5 h	μ	$a = 498.7$; $c = 2733$	52.6 ± 0.5	32.8 ± 0.9
19	80.6 ± 0.7	13.1 ± 0.7	as-cast	**A2**(Ta)	$a = 327.6$	92.1 ± 1.5	5.1 ± 0.6
				μ	$a = 501.5$; $c = 2760$	56.3 ± 1.1	28.6 ± 0.2
				eutectic	–	58.5 ± 1.0	27.3 ± 0.8
			1973 K/5 h	A2(Ta)	$a = 328.0$	91.5 ± 1.8	5.3 ± 1.2
				μ	$a = 500.9$; $c = 2745$	54.5 ± 0.4	33.1 ± 0.7
				σ	$a = 990.0$; $c = 519.8$	77.5 ± 1.0	13.3 ± 0.6
20[g]	2.0 ± 0.2	73.5 ± 0.5	as-cast	**A2**(Fe)	$a = 291.6$	1.8 ± 0.7	73.9 ± 1.1
				λ	[c]	27.4 ± 0.5	58.1 ± 0.6
			UDS	A2	$a = 291.4$	2.0 ± 0.4	72.3 ± 0.6
				quenched liquid	–	3.9 ± 0.3	69.6 ± 0.3
			1673 K/5 h	A2(Fe)	$a = 291.5$	2.0 ± 0.2	73.7 ± 0.5
			UDS + 1123 K/362 h	A2(Fe)	$a = 291.5$	0.77 ± 0.08	73.7 ± 0.5
				λ	$a = 485.4$; $c = 789.8$	28.2 ± 1.2	62.4 ± 0.4
			1673 K/5 h + 923 K/ 482 h	B2	$a = 291.4$	[d]	
				λ	$a = 485.4$; $c = 789.7$	[d]	
			UDS + 823 K/362 h	A2(Fe)	$a \approx 292$	[d]	
				$L2_1$	$a \approx 581$	[d]	

[a] For the as-cast samples, a phase given in *bold font* is the primary one

[b] For the lattice parameters given with symbol '=', the relative error is ±0.03 and ±0.05 % for cubic and for all other structures, respectively. For the lattice parameters given with symbol '≈', the absolute error is ±1 pm

[c] Small amount, at the limit of XRD detection

[d] Too little grains/precipitates for EDS measurements

[e] Owing to the small fraction of the bcc phase, it was impossible to discriminate between the W (A2) and the CsCl (B2) crystal structure types. Taking into account the information of [11, 23, 24], the B2 type was presumed

[f] Small amount of non-equilibrium phase formed upon cooling below 1420 K

[g] The sample also contains 0.2 at.% C

Microanalysis system, Oxford Instruments). Phase composition measurements were carried out at an accelerating voltage of 15 kV and a working distance of 10.5 mm, mainly by means of spot measurements. The integral composition was determined as average from at least 3 EDS measurements taken within rectangular frames of adequate size, e.g. 600 μm × 400 μm. The acquired EDS spectra were evaluated against an own standard with composition close to the equiatomic TaFeAl, initially determined by wet chemical analysis. The averaged chemical composition of the alloys and the coexisting phases in all as-cast and annealed samples are listed in Table 2. The table also includes the composition of eutectic structure constituents being measured by EDS within frames of adequate size, whenever applicable.

SEM micrographs of the as-cast samples (left column) and samples annealed at subsolidus temperatures (right column), all from group (i) containing about 13 at.% Ta,

reveal the C14 Laves (λ) phase as major constituent (Fig. 1).[2] In the as-cast condition, all samples show primary dendrites of the Laves phase, i.e. up to 73.4 at.% Al. The two-phase A2(Fe)(black) + λ(white) eutectic is clearly observed in the sample no. 3 (Fig. 1a, left). Sample no. 7 displays primary Laves dendrites and interdendritic Fe_2Al_5 grains decorated with a fine, terminal eutectic (Fig. 1c, left). After subsolidus annealing, the samples no. 3 and no. 1 shown in Fig. 1a, b on the right side display a two-phase microstructure consisting of A2(Fe)(black) + λ(white), the annealed sample no. 7 (Fig. 1c, right) consists of Fe_2Al_5(black) + λ(white), while sample no. 5 (Fig. 1d, right) is composed of three phases Fe_4Al_{13}(black) + λ(grey) + ε(white).

The microstructures of the as-cast and annealed samples (subsolidus annealing) from group (ii) containing about 32 at.% Ta are displayed in Fig. 2 and indicate that the homogeneity range of the C14 Laves phase is particularly extended. Few bright particles were identified to be fcc $(Ta_{1-x}Fe_x)C_{1-y}$ carbide inclusions [29], originating from carbon impurities. Sample no. 11 (Fig. 2d) contains about 15 vol.% of ε, 85 vol.% of λ and traces of Fe_4Al_{13}. The last phase is found both in the as-cast condition and also after annealing for 6 h at 1723 K. Since the sample composition is practically in the ε–λ tie-line, we can assume that Fe_4Al_{13} is formed as non-equilibrium phase upon cooling below 1420 K. The microstructures of samples from group (iii) with about 53 at.% Ta are displayed in Fig. 3 and indicate the wide homogeneity range of the μ phase. Sample no. 18 is nearly composed of single μ phase in the as-cast state and certainly after subsolidus annealing (Fig. 3a). Sample no. 17 with 23.6 at.% Al consists of μ + σ, the primary and major phase is the plate-like μ, the plates being separated by very thin layers of σ (Fig. 3b). The as-cast sample no. 16 contains primary σ dendrites enveloped by μ. After subsolidus annealing, its microstructure contains coarsened σ that appears more rounded being embedded in the μ phase matrix (Fig. 3c).

Sample no. 20 ($Ta_{2.0}Fe_{73.5}Al_{24.3}C_{0.2}$) shows the expected dendritic A2(Fe) solidification structure with pronounced segregation of Ta (Fig. 4a). The same alloy was subjected to unidirectional solidification (UDS) followed by quenching: the microsegregation pattern is clearly visible in the transverse section through the quenched mushy zone in Fig. 4b. In the interdendritic region, there is a minor amount of carbide particles (too few for detection by XRD) and substantial amount of non-equilibrium Laves phase formed due to the strong segregation of Ta. The carbides seem to be fcc $(Ta_{1-x}Fe_x)C_{1-y}$, where $x \approx 0.05$ and $y \approx 0.3$, as reported by Schneider et al. [29] for the alloy $Ta_{2.0}Fe_{71.0}Al_{26.0}C_{1.0}$. After annealing at 1673 K for 5 h, the non-equilibrium Laves phase dissipated and the microstructure consists of few large A2(Fe) grains and a small amount of tiny (1,…, 5 μm) carbide particles (Fig. 4c). After further annealing at 1123 K for 362 h and 923 K for 482 h, the sample shows plate-like precipitates inside the (Fe) matrix, identified by XRD as Laves phase. After annealing at 823 K for 362 h (subsequent to annealing at 1673 K for 5 h followed by quenching in Ga), no precipitates are visible in SEM (Fig. 4f), but a little amount (2.3 %) of the Heusler phase $L2_1$ was identified by XRD (see 'XRD analysis of samples' section).

The microstructure of samples no. 1–3 was investigated after annealing at 1123 K for 744 h and at 923 K for 482 h (Fig. 5a–c). The microstructure consists of mainly a matrix of A2 or B2 and grains of Laves phase. The X-ray diffractogram of sample no. 1 shows that only traces of the Heusler phase $L2_1$ may be assumed to form during annealing at 923 K for 482 h (see 'XRD analysis of samples' section).

XRD analysis of samples

XRD measurements were carried out in a DRON-3 (Burevestnik, Inc., St. Petersburg, Russia) diffractometer on powder samples or on coarse grained samples for Fe-rich alloys. The X-ray diffractograms of the as-cast samples and samples annealed at subsolidus temperatures (see Table 2) were recorded using the Cu–K_α filtered radiation at an angular step of $2\theta = 0.05°$ and an exposure of 8 s. For the samples annealed at 1123 K for 744 h, at 923 K for 482 h and at 823 K for 362 h, the Cu–$K_{\alpha 1}$ monochromatic radiation was used, and the exposure time was increased up to 30 s. The obtained data are also summarized in Table 2. The phase constituents identified by XRD are fully consistent with the results from SEM/EDS analysis.

X-ray diffractograms were carefully analysed with respect to the presence of the Heusler phase in samples no. 1 and 20 after low temperature annealing treatments. Unfortunately, little is known about the lattice parameters and site occupation of the $L2_1$ phase $TaFe_2Al$; based on theoretical calculations, Mekhrabov and Akdeniz [27] predicted that Ta atoms preferentially substitute the Fe sublattice sites in $Ta_xFe_{50}Al_{50-x}$, while Bozzolo et al. [26] suggested the substitution of Al sublattice sites by Ta for $Ta_xFe_{50-x}Al_{50}$ and $Ta_xFe_{50}Al_{50-x}$ alloys. Anthony and Fultz [25] experimentally established that in the $L2_1$ phase, Ta atoms occupy the 4(*b*) Wyckoff sites (1/2, 1/2, 1/2), rather than 8(*c*) with Fe or 4(*a*) with Al. It is worth noting that only the difference in the occupation of 4(*a*) and 4(*b*) Wyckoff positions distinguishes the $L2_1$ and the B2 structures. Hence, the smaller the difference of the averaged atomic weights in 4(*a*) and 4(*b*) sites, the smaller the intensity of the superstructure reflections with odd indexes

[2] In Figs. 1, 2 and 3, the microstructures in columns are presented in increasing of Al content.

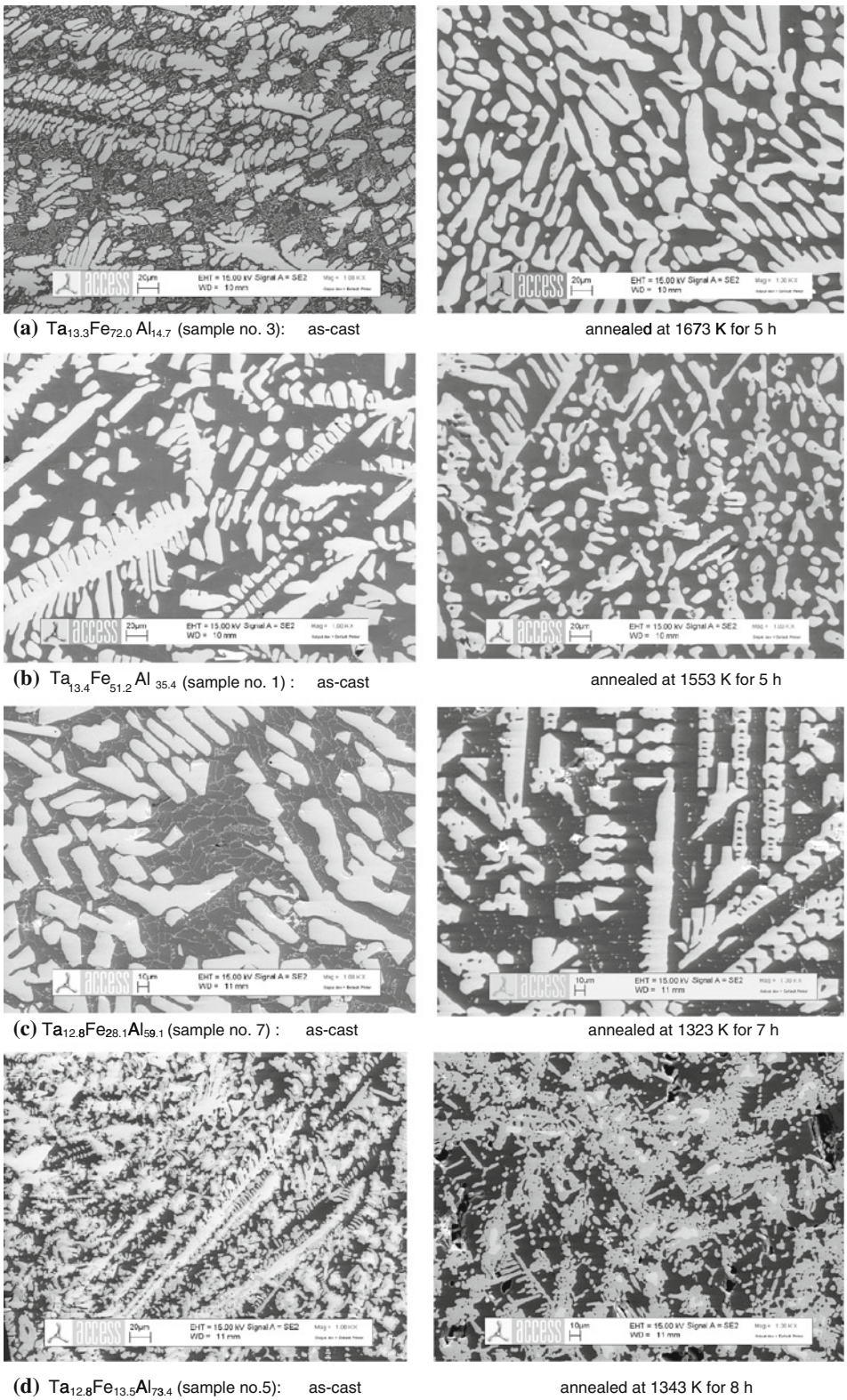

Fig. 1 SEM/BSE micrographs of the as-cast alloys (*left column*) and samples annealed at subsolidus temperatures (*right column*) reveal the following microstructure constituents: A2(Fe)(*dark*) + λ(*white*) in sample no. 3 (**a**) and no. 1 (**b**); Fe_2Al_5(*dark*) + λ(*white*) and tiny eutectic grains in sample no. 7 (**c**) and Fe_4Al_{13}(*dark*) + λ(*grey*) + ε(*white*) in sample no. 5 (**d**). Few very bright particles in (**a**–**c**) are carbide inclusions originated from carbon impurities. Annealing conditions and phase compositions are given in Table 2

(111), (311), etc., characteristic for $L2_1$, will be. In the present study, the lattice atom occupation for the $L2_1$ phase was taken from [25] with Al, Fe, Ta on the 4(*b*) position. The site fractions for this phase for the temperatures of interest were obtained by thermodynamic calculations by means of the proposed description.

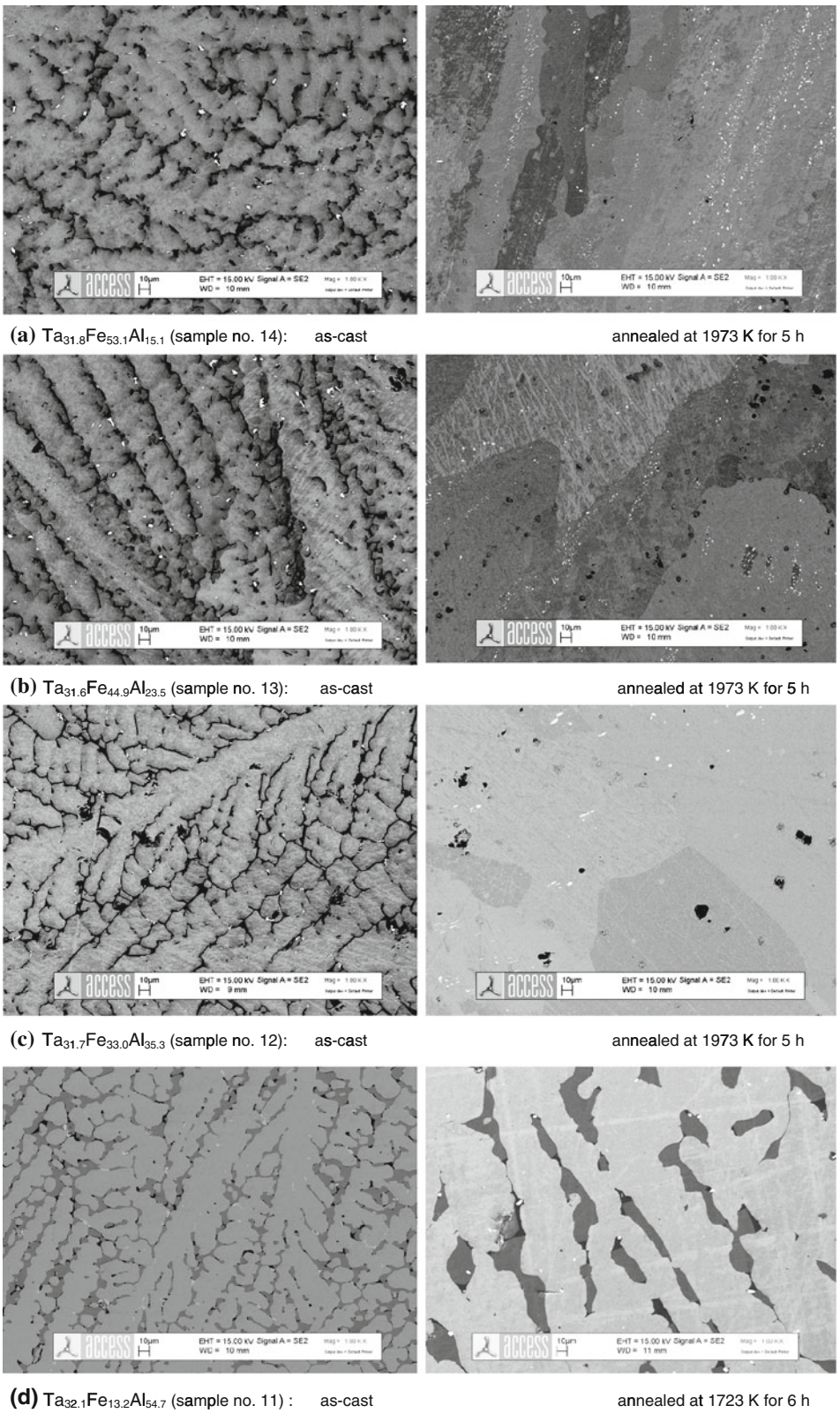

Fig. 2 SEM/BSE micrographs of the as-cast alloys (*left column*) and samples annealed at subsolidus temperatures (*right column*) reveal the following microstructure: λ(*light grey*) with significant microsegregation in samples no. 14 (**a**), no. 13 (**b**) and no. 12 (**c**); λ(*light grey*) + ε(*dark grey*) in sample no. 11 (**d**). *Black areas* in (**b**) and (**c**) correspond to porosity. Very bright particles are carbide inclusions originated from carbon impurities. In (**a**) and (**b**), small fraction of non-equilibrium μ phase and in (**d**) traces of non-equilibrium Fe_4Al_{13} phase formed below 1420 K during cooling were detected. Annealing conditions and phase compositions are given in Table 2

By means of illustration, Fig. 6 shows fragments of the full profile analysis by Powder Cell (version 2.4) software for sample no. 1 ($Ta_{13.4}Fe_{51.2}Al_{35.4}$) annealed at 923 K for 482 h and sample no. 20 ($Ta_{2.0}Fe_{73.5}Al_{24.3}C_{0.2}$) annealed at 923 K for 482 h and at 823 K for 362 h. In Fig. 6a, the characteristic peaks (111) and (311) of $L2_1$ do not appear

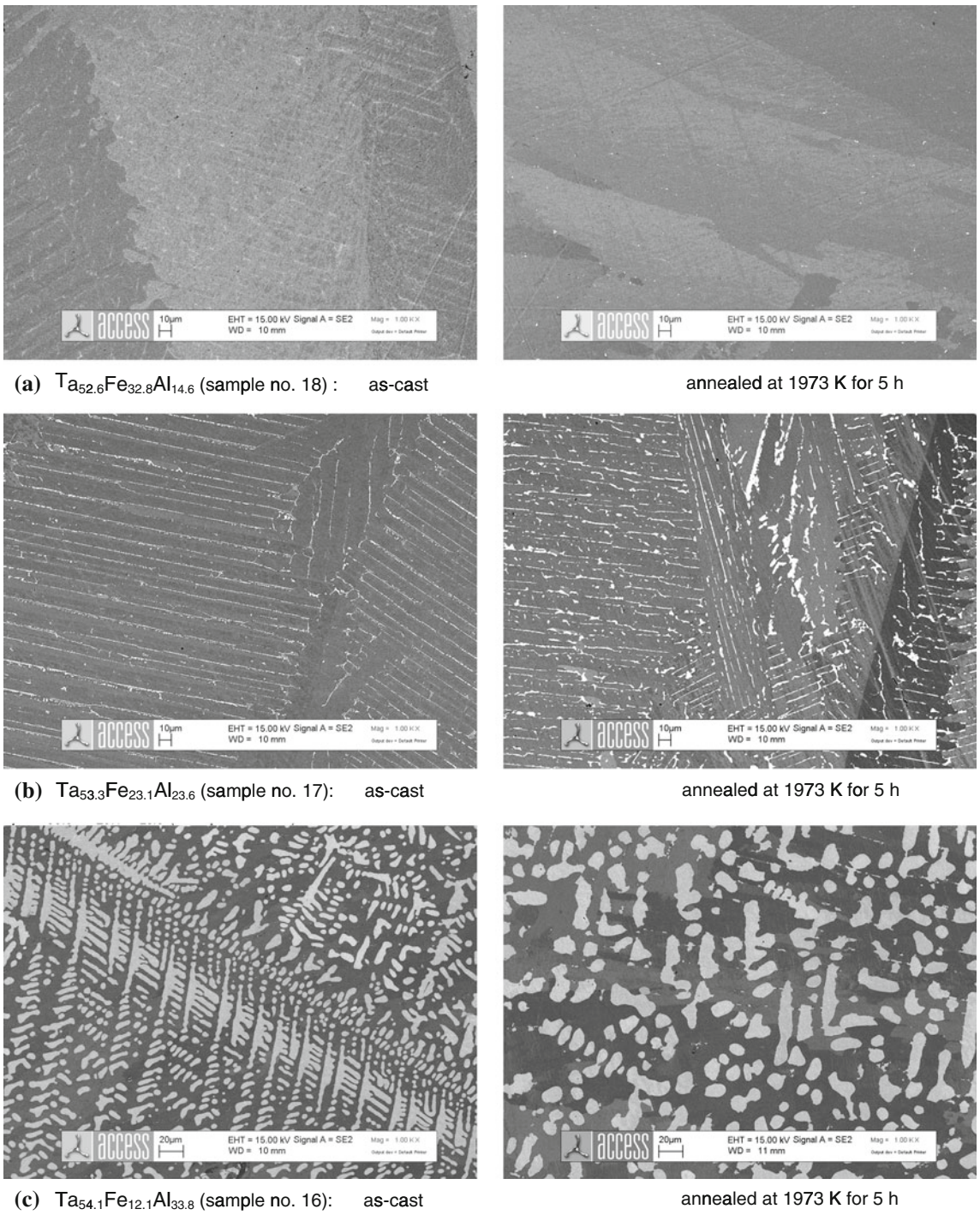

Fig. 3 SEM/BSE micrographs of the as-cast alloys (*left column*) and samples annealed at subsolidus temperatures (*right column*) reveal the following microstructure constituents: $\mu(grey)$ in sample no. 18 (**a**); $\mu(grey) + \sigma(bright)$ in samples no. 17 (**b**) and no. 16 (**c**). In (**b**) and (**c**), small fraction of non-equilibrium λ precipitates formed during cooling was detected by XRD. Annealing conditions and phase compositions are given in Table 2

unambiguously from the background and accordingly the fraction of the $L2_1$ phase is either small or the phase is entirely absent. The Rietveld refinement for the sample no. 20 annealed at 923 K for 482 h (Fig. 6b) shows no $L2_1$ phase, but only 95 % B2 + 5 % λ, while the same sample annealed at 823 K for 362 h (Fig. 6c) is composed of ~98 % A2 + ~2 % $L2_1$ with Laves phase being absent.

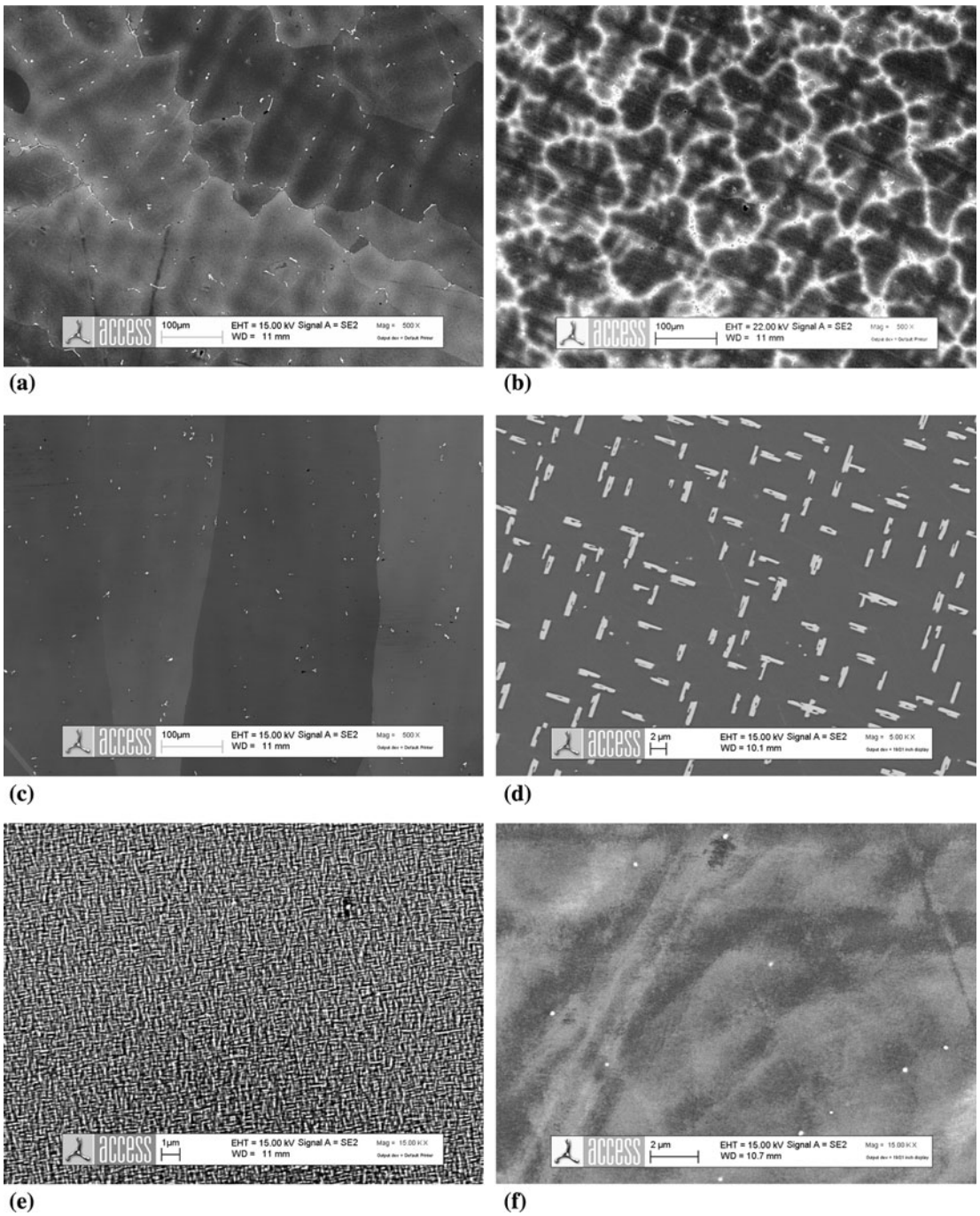

Fig. 4 SEM/BSE micrographs of sample no. 20 ($Ta_{2.0}Fe_{73.5}Al_{24.3}C_{0.2}$) in the as-cast state (**a**) and after unidirectional solidification (UDS) in transverse section (**b**); after annealing UDS sample at 1673 K for 5 h (**c**), at 1123 K for 362 h (**d**), at 923 K for 482 h (**e**) and at 823 K for 362 h (**f**). Very bright particles/areas correspond: **a** to carbides and non-equilibrium Laves phase, **b** to quenched liquid enriched with Ta, **c** and **f** to carbides, **d** and **e** to Laves phase precipitates. In **f**, no precipitates were visible in SEM, but XRD (see 'XRD analysis of samples' section) reveals the presence of A2 and $L2_1$

Lattice parameters of the λ and μ phases were evaluated as function of the aluminium content. The results are shown in Fig. 7: the solubility of Al in λ extends up to 52 at.% Al and up to 36 at.% in μ, both at subsolidus temperatures. The lattice parameters of the λ phase are in excellent agreement with data reported by Von Keitz et al. [21] for the composition range from 0 to 35 at.% Al.

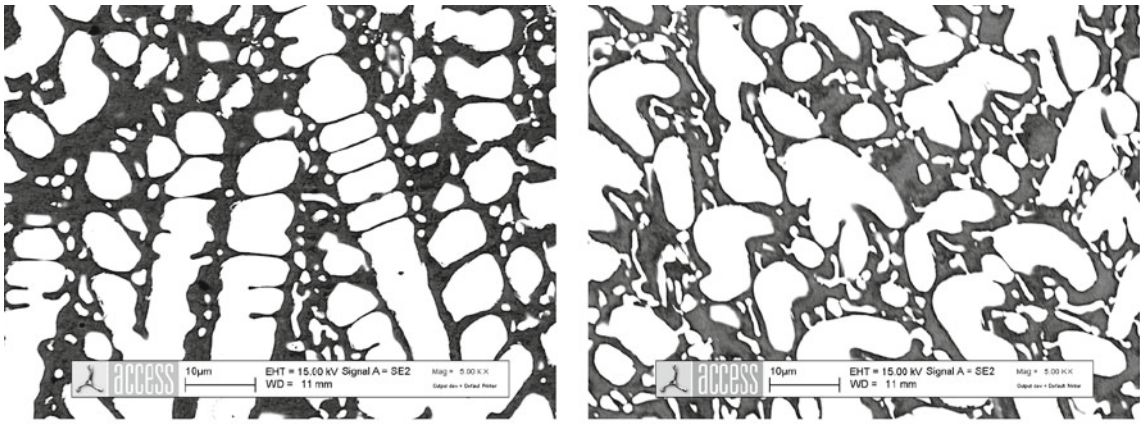

(a) $Ta_{13.3}Fe_{72.0}Al_{14.7}$ (sample no. 3)

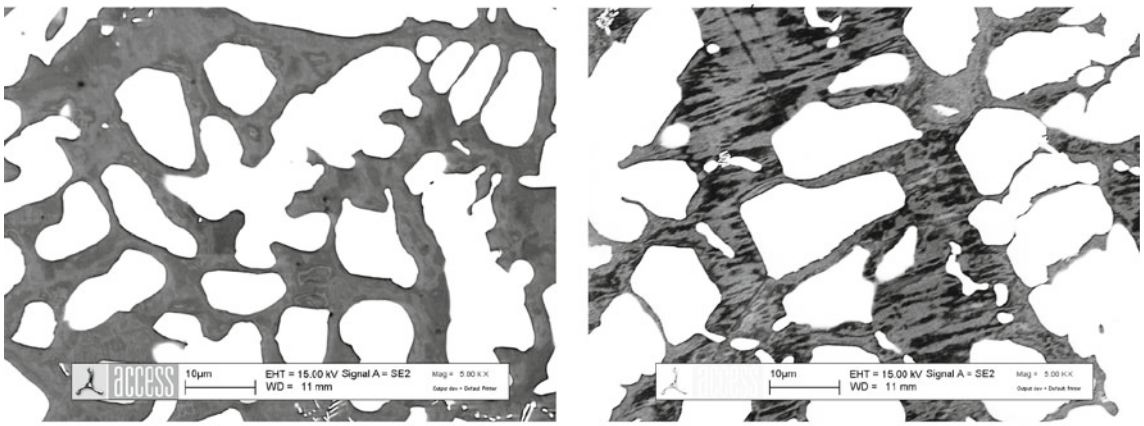

(b) $Ta_{13.5}Fe_{62.5}Al_{23.9}$ (sample no.2)

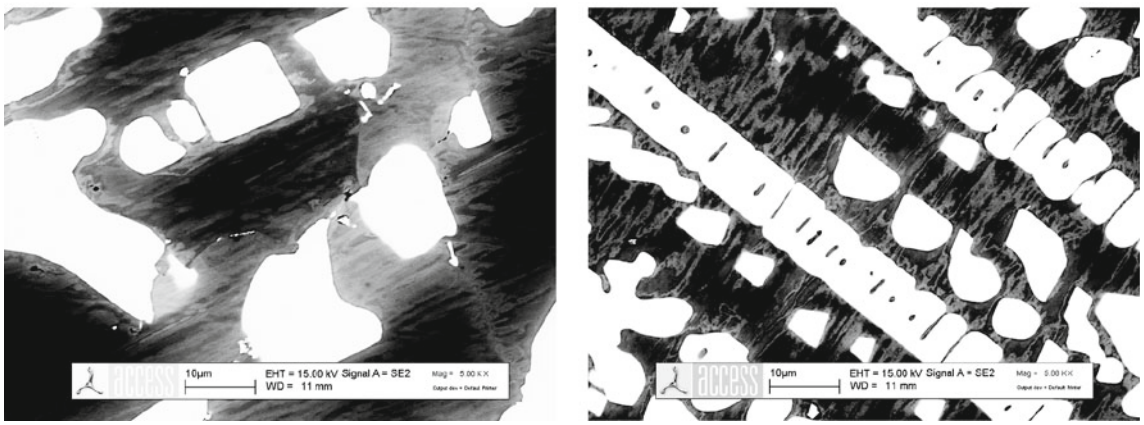

(c) $Ta_{13.4}Fe_{51.2}Al_{35.4}$ (sample no. 1)

Fig. 5 SEM/BSE micrographs of samples annealed at 1123 K for 744 h (*left column*) and at 923 K for 482 h (*right column*) reveal the following microstructure constituents: λ(*bright*) and (Fe)-matrix (*black*). In (**c**)XRD (see 'XRD analysis of samples' section) revealed the presence of $L2_1$, assumed to be nanosized precipitates inside the B2(Fe) matrix

DTA and DSC analysis of transformation temperatures

Temperatures of solid-state and solid–liquid phase transformations for the as-cast samples and samples annealed at subsolidus temperatures were determined by DTA using Sc_2O_3 crucibles for samples in the range rich in Ta (≥32 at.%) and lean in Al (<40 at.%) and Al_2O_3 crucibles for all other samples. The high temperature DTA apparatus (max. temperature 2500 K) was equipped with W/W-20Re string thermocouples designed by Kocherzhinskiy et al. [30, 31].

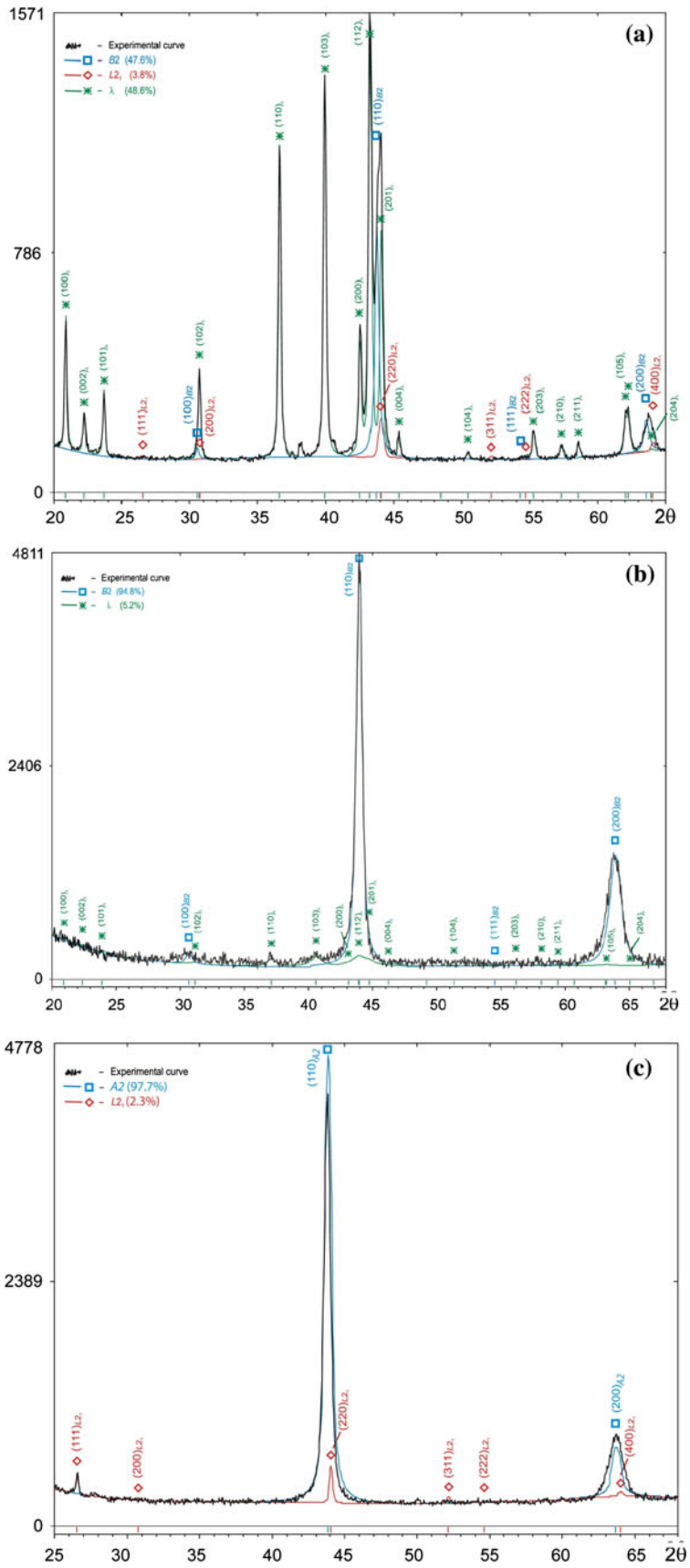

Fig. 6 (Colour online). Fragments of the full profile analysis of diffractograms for sample no. 1 ($Fe_{51.2}Ta_{13.4}Al_{35.4}$) annealed at 923 K for 482 h (**a**), sample no. 20 ($Fe_{73.7}Ta_{2.0}Al_{24.3}C_{0.2}$) annealed at 923 K for 482 h (**b**) and the same annealed at 823 K for 362 h (**c**)

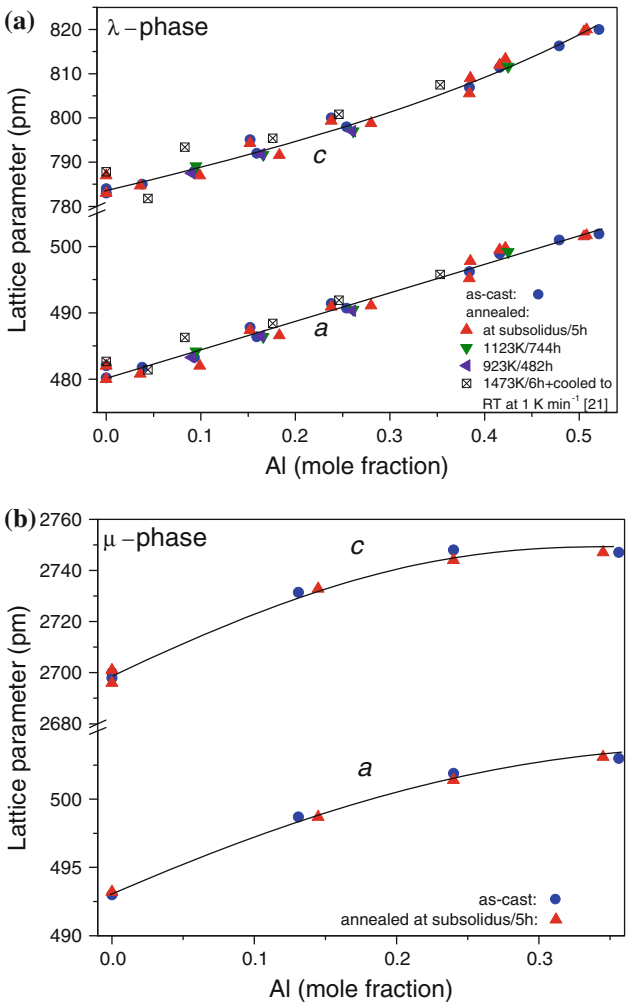

Fig. 7 (Colour online). Variation of lattice parameters as a function of the Al content in sample series consisted mainly of λ phase (**a**) and μ phase (**b**). In (**a**) data reported by Von Keitz et al. [21] are also included

The DTA measurements were performed under high purity He atmosphere with heating and cooling rates of 20 K min^{-1}. The thermocouple was calibrated using the International Temperature Scale of 1990 reference points of Al, Au, Pd, Pt, Rh and additional reference points of Fe and Al_2O_3. After calibration, the reproducibility of phase transformation temperatures of these references was evaluated to be about ±0.5 %. During the evaluation of phase transformation temperatures from the recorded DTA curves, the practical guide on differential thermal analysis of metals and alloys recommended by the National Institute of Standards and Technology [32] was followed.

DTA measurements were performed first for the as-cast samples. This allowed selecting an appropriate temperature for subsolidus annealing. DTA measurements were repeated for all annealed samples, the results being summarized in Table 3, along with the values calculated using the proposed thermodynamic description of the Al–Fe–Ta system. Hence, we have used the so-called 'hybrid approach' that has been applied quite successfully for the study of phase equilibria and phase transformations in many systems. It consists of performing experimental investigations of phase equilibria in parallel with thermodynamic modelling. Therefore, our interpretation of the DTA results in Table 3 was guided by thermodynamic calculations performed throughout the CALPHAD assessment. To underline this, we explicitly included in Table 3 the column 'Phase transformation' into the block labelled 'Results of calculation'.

By means of the illustration, DTA curves recorded upon heating and cooling are displayed in Fig. 8 for few selected samples. The curve of alloy no. 9 is meant to illustrate the resolution DTA signals at heating and cooling rates of 20 K min^{-1}. The complex cascade of transformations, taking place in the temperature range 1369–1445 K within an interval of 76 K, can be well resolved to yield four independent peaks/signals. The resolution is especially good upon cooling. Only the heating curves were used for determining transformation temperatures since undercooling effects were observed during solidification, which were in many cases associated with strong recalescence (see, for example, the DTA curve upon cooling for the alloy no. 18 in Fig. 8).

From the recorded DTA data, it is possible to conclude that the ternary system comprises a quasi-binary eutectic reaction, L ⇆ A2 + λ, at a temperature 1733 K or somewhat higher (see the alloy no. 4 in Table 3). This can be inferred from the fact that the solidus temperatures first rise with increasing Al content compared to the Fe–Ta binary alloys (see [13]), then reach the maximum value in the range of 7–15 at.% Al before decreasing again as the Al content continues to increase. Just the same behaviour is observed for the alloys with 53–54 at.% Ta being close to the homogeneity range of μ-phase (see the alloy no. 18 in Table 3).

A series of DSC measurements was performed with alloys no. 1–3 annealed at 1123 K and alloy no. 20 annealed at 1123, 923 and 823 K using a PyrisTM DSC-7 (PerkinElmer, Inc., Massachusetts, USA) calorimeter operating in temperature range from 300 to 1000 K. The calorimeter was calibrated by measuring the melting point of high purity Al and the heat capacity of a reference sample (sapphire disc) supplied by Perkin-Elmer. For each DSC-run, a sample of 130 ± 10 mg was used. After introducing the sample into the DSC furnace and sealing the furnace tightly, the excess pressure of the inner gas (Ar with purity 6 N) in the furnace automatically rose to about 100 Pa. The heating and cooling rate of 10 K min^{-1} was found best for observing solid-state transformations. Several heating/cooling cycles were applied for each selected

Table 3 Phase transformation temperatures measured in the Al–Fe–Ta samples by DTA and DSC with a rate of 20 and 10 K min^{-1}, respectively

No.	Composition, at.%	DTA measurements, K		Results of calculation	
		Heating	Cooling	*T*, K	Phase transformation
1	$Ta_{13.4}Fe_{51.2}Al_{35.4}$	–[a], 1982	–, 1939	1958	L\L + λ (liquidus)
		1640, 1627	1616, 1603	1637	L + λ\L + A2 + λ[b]
		1608, 1590	1589, 1577	1613	L + A2 +λ\A2 + λ (solidus)
		–, 1577	–	1555	A2 +λ\A2 + B2 + λ
		1597, 1477	–	1543	A2 + B2 + λ\B2 + λ
		950 ± 20[c]	–	959	$L2_1$ + λ\$L2_1$
2	$Ta_{13.5}Fe_{62.5}Al_{23.9}$	1958	1952	1951	L\L + λ (liquidus)
		–	1687	1706	L + λ\L + A2 + λ
		1687	–	1701	L + A2 +λ\A2 + λ (solidus)
		1246	–	1226	A2 +λ\B2 + λ
		940 ± 20[c]	–	907	B2 + λ\B2 + $L2_1$ + λ
		845 ± 20[c]	–	840	B2 + λ ⇆ $A2^{fm}$ + $L2_1^d$ (U_{14})
		565 ± 20[c]	–	557	$A2^{fm}$ + $L2_1$ ⇆ $D0_3^{fm}$ + $L2_1^{fm}$ (U_{M5})
3	$Ta_{13.3}Fe_{72.0}Al_{14.7}$	1968, 1964	1964, 1951	1941	L\L + λ (liquidus)
		–	1724, 1717	1733	L + λ\L + A2 + λ
		1729, 1726	–	1732	L + A2 + λ\A2 + λ (solidus)
		936,920,953 ± 20[c]	–	943	A2 + λ\$A2^{fm}$ + λ
		810 ± 20[c]	–	725	$A2^{fm}$ + λ\$A2^{fm}$ + $L2_1$ + λ
		582 ± 20[c]	–	569	$A2^{fm}$ + $L2_1$ + λ ⇆ $L2_1^{fm}$ (P_M)
4	$Ta_{12.8}Fe_{80.4}Al_{6.8}$	1967	1964	1923	L\L + λ (liquidus)
		–	1719	1737	L + λ\L + A2 + λ
		1733	–	1736	L + A2 +λ\A2 + λ (solidus)
		1041	–	1032	A2 + λ\$A2^{fm}$ + λ
5	$Ta_{12.8}Fe_{13.5}Al_{73.4}$[a]	1659, 1673	1650, 1675	1684	L + λ\L + ε + λ
		–	–	1553	L + ε + λ\L + ε
		–	1375, 1381	1415	L + ε\L + ε + Fe_4Al_{13}
		1402, 1403	–	1408	L + ε ⇆ Fe_4Al_{13} + λ (U_8) (solidus)
		1250, 1177	–	1128	Fe_4Al_{13} + λ + ε\Fe_4Al_{13} + ε
6	$Ta_{13.0}Fe_{21.4}Al_{65.7}$	1893, 1893	1880, 1893	1802	L\L + λ (liquidus)
		–	1368, 1369	1512	L + λ\L + ε + λ
		1403, 1404	–	1408	L + ε ⇆ Fe_4Al_{13} + λ (U_8) (solidus)
		931, 968	–	934	Fe_4Al_{13} + λ ⇆ $FeAl_2$ + ε (U_{12})
7	$Ta_{12.8}Fe_{28.1}Al_{59.1}$	1925	1912	1872	L\L + λ (liquidus)
		–	1371	1405	L + λ\L + λ + $FeAl_2$
		1404	–	1404	L ⇆ Fe_2Al_5 + $FeAl_2$ + λ (E_2) (solidus)
8	$Ta_{12.3}Fe_{30.0}Al_{57.7}$	1921	1917	1876	L\L + λ (liquidus)
		..	1405	1417	L + λ\L + Fe_5Al_8 + λ
		1412	1389	1406	L + Fe_5Al_8⇆$FeAl_2$ + λ (U_9) (solidus)
		1394	1366	1380	Fe_5Al_8 + $FeAl_2$ + λ\$FeAl_2$ + λ
9	$Ta_{12.7}Fe_{32.2}Al_{55.1}$	1941, 1930	1925, 1914	1901	L\L + λ (liquidus)
		1445, 1439	1424, 1427	1435	L + λ\L + Fe_5Al_8 + λ
		1424, 1419	1387, 1387	1414	L + Fe_5Al_8 + λ\Fe_5Al_8 + λ (solidus)
		1412, 1409	1366, 1367	1397	Fe_5Al_8 + λ\Fe_5Al_8 + $FeAl_2$ + λ
		1369, 1373	1334, 1339	1375	Fe_5Al_8 ⇆ B2 + $FeAl_2$ + λ (E_3)
10	$Ta_{13.2}Fe_{36.1}Al_{50.7}$	1949, 1947	1946, 1937	1933	L\L + λ (liquidus)
		1465, 1465	1459, 1459	1486	L + λ\L + B2 + λ
		1390, 1420	1360, 1373	1441	L + B2 ⇆ Fe_5Al_8 + λ (U_7) (solidus)
		1360, 1363	1330, 1337	1375	Fe_5Al_8 ⇆ B2 + $FeAl_2$ + λ (E_3)

Table 3 continued

No.	Composition, at.%	DTA measurements, K		Results of calculation	
		Heating	Cooling	*T*, K	Phase transformation
11	$Ta_{32.1}Fe_{13.2}Al_{54.7}$	1994	1968	1954	L\L + λ (liquidus)
		1795	1726	1807	L + λ\λ (solidus)
		1682	–	1640	λ\ε + λ
		1388[e]	–	–	–
12	$Ta_{31.7}Fe_{33.0}Al_{35.3}$	≤2104	2004	2112	L\L + λ (liquidus)
		2052	–	2099	L + λ\λ (solidus)
13	$Ta_{31.6}Fe_{44.9}Al_{23.5}$	≤2114	2056	2119	L\L + λ (liquidus)
		2053	–	2097	L + λ\λ (solidus)
14	$Ta_{31.8}Fe_{53.1}Al_{15.1}$	≤2116	1976	2108	L\L + λ (liquidus)
		2029	–	2058	L + λ\L + λ + μ (solidus)
15	$Ta_{37.4}Fe_{14.8}Al_{47.8}$	1995	1933	1987	L\L + λ (liquidus)
		–	–	1962	L + λ\L + λ + μ
		1925	1911	1926	L + μ ⇆ λ + σ (U_2)
		1905	1888	1919	L + λ + σ\λ + σ (solidus)
		–	–	1787	λ + σ\φ + λ + σ
		1798	–	1780	φ + λ + σ\φ + λ
16	$Ta_{54.1}Fe_{12.1}Al_{33.8}$	2134	2125	2120	L\L + σ (liquidus)
		2035	2017	2061	L + σ\L + μ+σ
		2017	–	2042	L + μ + σ\μ + σ (solidus)
17	$Ta_{53.3}Fe_{23.1}Al_{23.6}$	≤2096	2042	2094	L\L + μ (liquidus)
		2063	–	2087	L + μ\μ (solidus)
		–	–	2052	μ\μ + σ
18	$Ta_{52.6}Fe_{32.8}Al_{14.6}$	≤2102	2003	2088	L\L + μ (liquidus)
		2074	–	2083	L + μ\μ (solidus)
		1175	–	1088	μ\μ + σ
19	$Ta_{80.6}$ $Fe_{13.1}Al_{6.3}$[a]	2078	2069	2091	L + A2\L + A2 + σ
		2063	–	2066	L + σ ⇆ A2 + μ (U_1) (solidus)
20	$Ta_{2.0}Fe_{73.5}Al_{24.3}C_{0.2}$	1775	1754	1756	L\L + A2 (liquidus)
		1739	1721	1730	L + A2\A2 (solidus)
		1548	–	1531	A2\A2 + λ
		1145	–	1094	A2 + λ\B2 + λ
		929[f], 875 ± 20[c]	–	860	B2 + λ\A2 + B2 + λ
				840	B2 + λ ⇆ $A2^{fm}$ + $L2_1$ (U_{14})
				839	B2 + $L2_1$ ⇆ $A2^{fm}$ + $D0_3$ (U_{c2})
		740 ± 20[c]	–	759	$A2^{fm}$ + $D0_3$ ⇆ $D0_3^{fm}$ + $L2_1^{fm}$ (U_{M2})

All samples were annealed at subsolidus temperature (see Table 2). The results of calculations are given in the last two columns

[a] Sample was not completely melted

[b] Symbol '\' denotes crossing of phase boundary

[c] DSC result for the samples annealed at 1123 K (alloys no. 1–3) and 823 K (alloy no. 20)

[d] Symbol '⇆' denotes an invariant reaction

[e] This exothermal event upon heating is caused by decomposition of the non-equilibrium Fe_4Al_{13} phase

[f] This signal in the sample quenched from 1623 K may also be related with magnetic transformation of metastable A2 phase

sample, aiming to detect the sequence of ordering reactions. The transformation temperatures determined by DSC are given in Table 3, but the values are rather tentative due to the aspect of the apparent heat capacity curves.

As an example, Fig. 9a, b display the DSC curves for alloy no. 20 in two annealing states at 1123 K and 823 K, respectively. These two states differ significantly owing to the apparent heat capacity (Cp) obtained upon heating in the first heating cycle. We think that this may relate to the presence of the $L2_1$ phase in the sample annealed at 823 K, but not in the one annealed at 1123 K. The cooling curves, however, look rather similar with respect to values of the

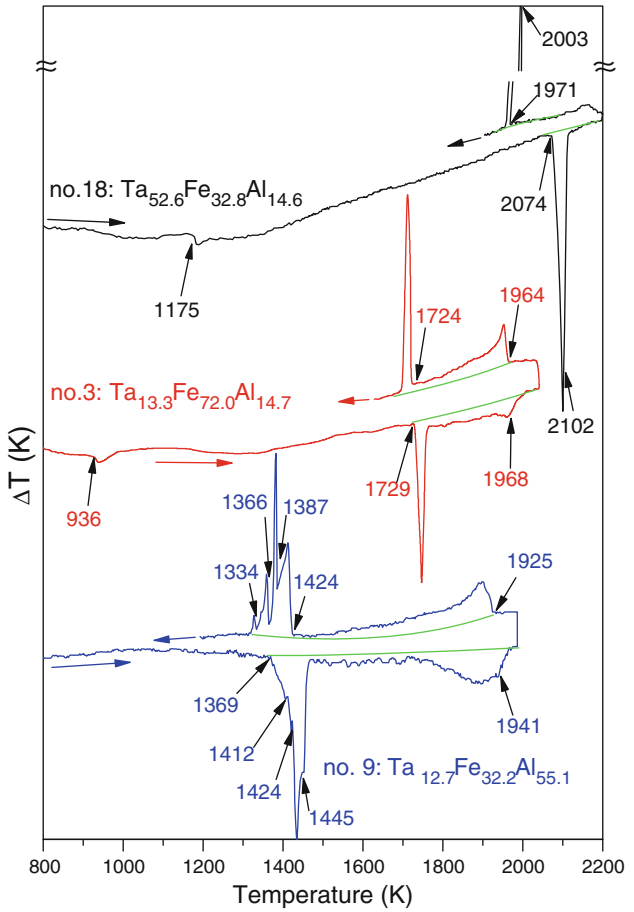

Fig. 8 (Colour online). Examples of DTA curves of few annealed Al–Fe–Ta samples recorded with a rate of 20 K min^{-1}. The annealing treatment being performed at subsolidus temperature for 5 h, followed by cooling at a rate of about 3 K s^{-1} (for clarity, the DTA curves have been shifted vertically)

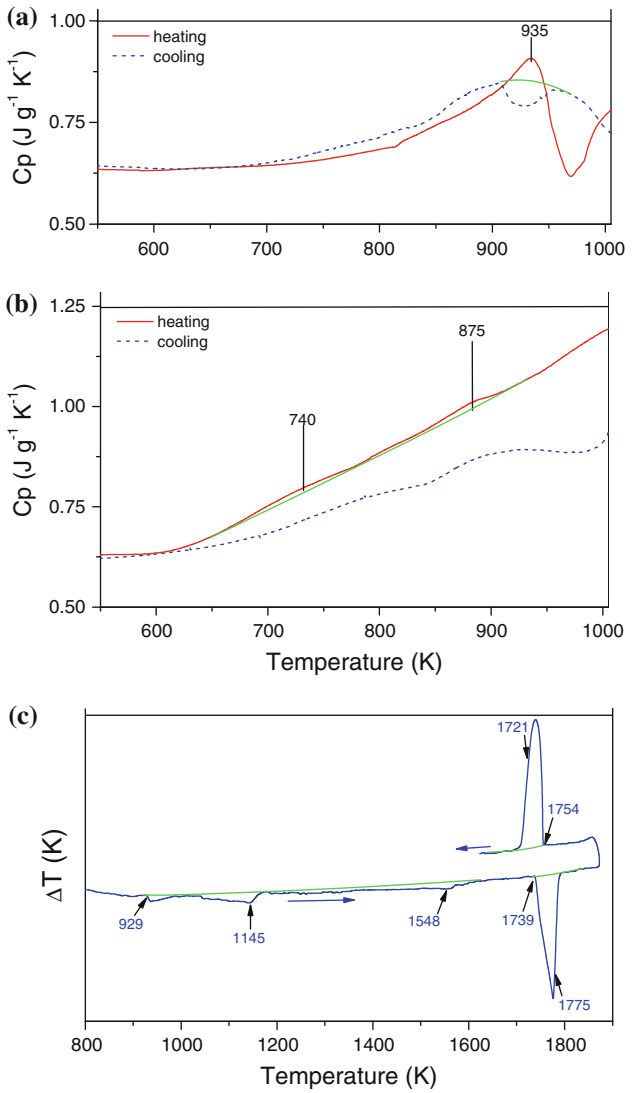

Fig. 9 (Colour online). Apparent heat capacity curves measured by DSC in first heating/cooling cycling run with a rate of 10 K min^{-1} for the sample no. 20 ($Ta_{2.0}Fe_{73.5}Al_{24.3}C_{0.2}$) annealed at 1123 K for 744 h (**a**) and at 823 K for 362 h (**b**) (after annealing the both samples were quenched in water), as well as DTA curve of this sample annealed at 1673 K for 5 h (followed by furnace cooling at a rate of about 3 K s^{-1}) recorded with a rate of 20 K min^{-1} (**c**)

apparent heat capacity. This may be attributed to the dissolution of the majority of the $L2_1$ precipitates in the course of heating to 1000 K. The peaks as such are interpreted as follows: in Fig. 9a, the peak at 935 K probably corresponds to the magnetic ordering of the A2-phase. Usually, magnetic transformations should only contribute to the entropic term of the Gibbs free energy; however, a small exothermic effect was found upon cooling and could not be fully understood. In Fig. 9b, the peak at 935 K is absent and only two weak and broad endothermal signals around 740 and 875 K are visible. They are attributed to a sequence of second-order transformations as listed in Table 3, based on thermodynamic calculations.

Dissolution calorimetry

Within the frame of the present study, the standard enthalpy of formation at 298 K was determined by isoperibolic drop calorimetry (IDC) on samples annealed at subsolidus temperatures (see Table 2). The selected samples contain as a major constituent the λ phase (samples no. 11–14) and the μ phase (samples no. 16–18). In order to find the sample variance and standard deviation, at least five pieces from each selected for the calorimetric investigation material were dissolved. Similar binary Fe–Ta alloys were measured previously [13]. The method is well described [33, 34] and involves the determination of the molar partial enthalpy of dissolution of pure solid Ni, Fe, Ta and Al, as well as that of the ternary Al–Fe–Ta alloys in liquid Ni by IDC. Each dissolution experiment was started by dropping several samples of pure Ni at 298 K into liquid Ni which is at 1773 ± 5 K. Nickel samples were dropped further after each dropping of Al and

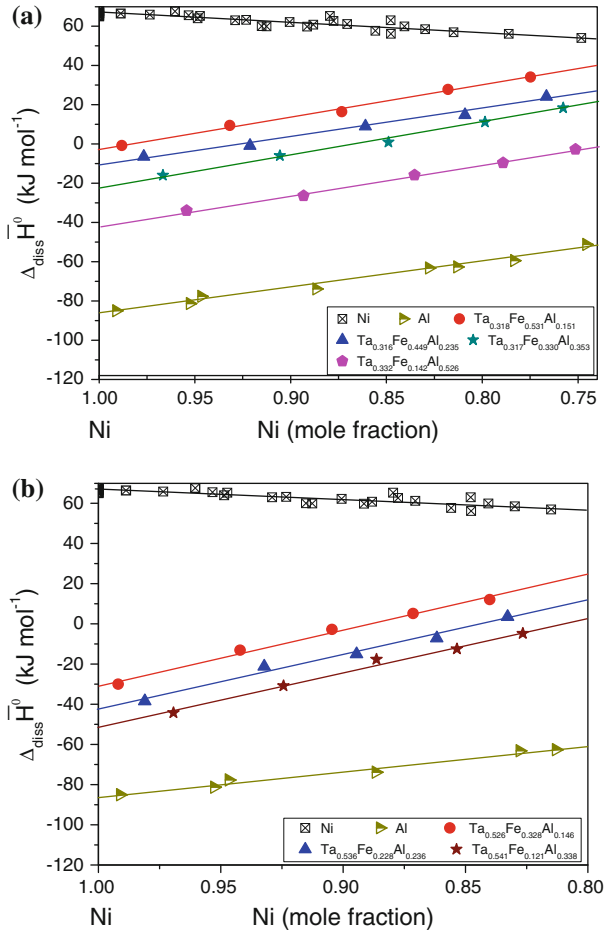

Fig. 10 (Colour online). Enthalpy of dissolution of cold samples (298 K) from pure elements Ni, Al and from selected Al–Fe–Ta alloys in liquid Ni at 1773 ± 5 K as function of molar fraction of the solvent. The selected ternary alloys consisted of the λ phase (**a**) and the μ phase (**b**) as single or major constituent

$Ta_{1-x-y}Fe_xAl_y$ alloys to determine the composition-dependent calibration factor. The enthalpy change upon heating Ni from room temperature to 1773 K was calculated by means of the Scientific Group Thermodata Europe (SGTE) database PURE4 [35, 36] yielding a value of 66.87 kJ mol^{-1}. The molar partial enthalpies of dissolution ($\Delta_{diss}\overline{H}_i$) of the samples and of pure Al are given in Fig. 10. For the elements Fe and Ta, the molar partial enthalpies of dissolution are determined in the same conditions, being reported in [13]. In the investigated composition ranges, the $\Delta_{diss}\overline{H}_i$ varies linearly with solvent composition. Due to this, the molar partial enthalpies of dissolution ($\Delta_{diss}\overline{H}_i$) of cold samples at infinite dilution ($x_{Ni} \rightarrow 1$) and their standard deviations ($2\sigma_i$) were obtained by means of linear fit of the measured values. The results are summarized in Table 4.

The standard enthalpies of formation ($\Delta_{298}H^0$) and their 2σ standard deviations for the $Fe_{1-x-y}Ta_xAl_y$ alloys, referred to bcc-Fe, bcc-Ta and fcc-Al at 298 K, were determined by means of the values from Table 4 and the following expressions:

$$\Delta_{298}H^0 = (1-x-y)\Delta_{diss}\overline{H}^0_{Ta} + x\Delta_{diss}\overline{H}^0_{Fe} + y\Delta_{diss}\overline{H}^0_{Al} - \Delta_{diss}\overline{H}^0_{Ta_{1-x-y}Fe_xAl_y} \quad (1)$$

$$2\sigma = \sqrt{\sum_i (n_i 2\sigma_i)^2} \quad (2)$$

The obtained values of the enthalpy of formation for one mole of formula unit of an alloy $Ta_{1-x-y}Fe_xAl_y$ are also presented in Table 4. From these data, a stabilizing effect of Al is evidenced for both ternary λ and μ phases: the standard enthalpies of their formation decreases with increasing Al content from −6 to about −23 kJ mol^{-1} and from −7 to about −17 kJ mol^{-1}, respectively. The composition dependencies of $\Delta_{298}H^0$ for λ-$Ta_{0.32}Fe_{0.68-x}Al_x$ and μ-$Ta_{0.53}Fe_{0.47-x}Al_x$ are shown and discussed in 'Thermodynamics properties' section based on thermodynamic calculations.

Thermodynamic models and optimization

The designation of individual phases, their crystal structure and the sublattice models for solid phases employed in the present thermodynamic description are summarised in Table 1. The Gibbs energy functions for the stable and metastable structures of the pure elements were adopted from the SGTE database compiled by Dinsdale [35, 36]. We used the thermodynamic models for the individual phases stemming from thermodynamic descriptions of the constituent binary systems Al–Fe [11], Al–Ta [12] and Fe–Ta [13]. The calculated phase diagrams of these constituent binary systems are illustrated in Fig. 11. The gas phase was included to allow extrapolation up to temperatures of 6000 K.

The model parameters for liquid and all solid phases of the ternary system Al–Fe–Ta were evaluated by searching for the best fit to available experimental phase equilibria and thermodynamic data by means of the PARROT optimiser of the software Thermo-Calc [37]. During the process of optimization for the liquidus and solidus temperatures determined in the present study (see Table 3), as well as for the analogous DTA data reported in Refs. [23, 24] were assigned a weight of 0.75 and 1.5, respectively, since the liquidus temperatures measured by conventional DTA are commonly less accurate than temperatures of solidus (the latter ones are routinely related with clear incipient melting points; for the former, it is difficult to select the actual thermal event [32]). A weight of 0.5 was fixed to the temperatures of incipient melting of the alloys measured by Pirani–Alterthum method [21]. For the tie-lines and tie-triangles of the present study (see

Table 4 Standard enthalpy of formation of Al–Fe–Ta alloys evaluated from dissolution enthalpy data measured by isoperibolic drop calorimetry

Samples	Molecular weight, g	Value, kJ mol^{-1}	
		$\Delta_{diss}\bar{H}^0 \pm 2\sigma$	$\Delta_{298}H^0 \pm 2\sigma$
Ni[a]	58.69	66.4 ± 0.7 (66.87 [33, 34])	–
Fe[a]	55.85	42.3 ± 1.4	0
$Ta_{0.322}Fe^{a}_{0.678}$	96.13	5.1 ± 1.5	−5.7 ± 1.8
$Ta_{0.318}Fe_{0.531}Al_{0.151}$	90.19	−2.6 ± 1.0	−16.9 ± 1.4
$Ta_{0.316}Fe_{0.448}Al_{0.236}$	88.59	−10.9 ± 1.5	−19.1 ± 1.8
$Ta_{0.317}Fe_{0.330}Al_{0.353}$	85.28	−21.9 ± 1.2	−23.5 ± 1.6
$Ta_{0.331}Fe_{0.143}Al_{0.526}$	82.10	−41.9 ± 1.0	−27.7 ± 1.7
$Ta_{0.523}Fe^{a}_{0.477}$	121.28	−20.2 ± 1.0	−7.1 ± 1.4
$Ta_{0.526}Fe_{0.328}Al_{0.146}$	117.62	−30.6 ± 1.6	−16.0 ± 1.8
$Ta_{0.533}Fe_{0.231}Al_{0.236}$	116.15	−42.4 ± 2.2	−16.7 ± 2.3
$Ta_{0.541}Fe_{0.121}Al_{0.338}$	113.82	−51.7 ± 2.0	−21.7 ± 2.1
Ta[a]	180.95	−90.8 ± 1.2	0
Al	26.98	−86.8 ± 1.1	0

Dissolution experiments were performed in liquid Ni at 1773 ± 5 K

[a] See also [13]

Table 2) and [23, 24], a weight of 1.25 was prescribed. All other data from the present study and literature [7, 23–25] were used with a weight equal 1.

For the description of B2, $D0_3$ and $L2_1$ ordering (bcc-based phases), as well as for $L1_0$ and $L1_2$ ordering (fcc-based phases), four-sublattice models based on the compound energy formalism were applied, as proposed in [11]. Ordering to B2, $D0_3$ or $L2_1$ can be accomplished through first- or second-order transformations, depending on the composition (see Fig. 11a). The model expressions for the molar Gibbs energy as functions of temperature and composition are given in references [11, 37, 38]. When applying the models to ordering reactions in the ternary Al–Fe–Ta system, one should bear in mind that the $D0_3$ (Fe_3Al) phase is the binary limitrophe form of the ternary Heusler $L2_1$ ($TaFe_2Al$) phase [39]. With the addition of small amounts of Ta, the Thermo-Calc software starts to label this phase as $L2_1$#1, while the ternary Heusler phase is labelled $L2_1$#2, according to distinct composition sets. To improve the readability of the reaction scheme and of relevant figures, we replaced $L2_1$#1, which has tiny solubility of Ta, with $D0_3$ and $L2_1$#2 with $L2_1$.

The complete thermodynamic database in Thermo-Calc format [37] is listed in the Appendix.

Results of modelling and discussion

Complete reaction scheme

In the Al–Fe–Ta system, chemical and magnetic ordering reactions are present and were included in the Scheil's reaction scheme (Fig. 12), following the procedure and designation described in [40]. The ordering reactions may be of second-order nature, but can turn into first-order transformations [11, 39–48] at critical composition and temperatures (points S/F) and vice versa (F/S). In order to distinguish between second-order and first-order reactions, the following notations are used, as proposed in [40]. A superscript 'fm' denotes ferromagnetic state of a phase. All first-order univariant reactions are represented by solid lines. All second-order univariant reactions are represented by dotted lines for chemical ordering and dash-dotted lines for magnetic ordering. All univariant second-order reactions are labelled such that the disordered and ordered phases are separated by a slash, e.g. $B2/D0_3 + L2_1$ or $A2/A2^{fm} + B2$. All first-order invariant reactions are contained in boxes drawn with thick lines. All invariant reactions, which involve ordering, are contained in boxes drawn with thin lines.

According to the scheme in Fig. 12, the ternary system Al–Fe–Ta hosts 26 first-order four-phase invariant reactions encompassing 18 reactions of U-type, 6 reactions of E-type, 1 reaction of P-type and 1 reaction of M-type (metatectic). The system also contains 10 so-called quasi-binary three-phase invariant reactions among which 8 are of e-type (e_1–e_3, e_5, e_{10}, e_{11}, e_{15} and e_{16}) and 2 are of p-type (p_4 and p_6). The compositions of coexisting phases engaged into invariant equilibria with the liquid phase are listed in Table 5.

All other invariant reactions involve chemical and/or magnetic ordering in distinct configurations, similar to the U- and P-type reactions and also to double degenerated D^2-type reactions. The classification and notation of degenerated reactions was initially proposed by Lukas et al. [49]. In order to underline that a reaction involves chemical ordering, a 'C' is added as a subscript to the conventional reaction symbol, e.g. E_C, U_C, P_C and D_C; for magnetic

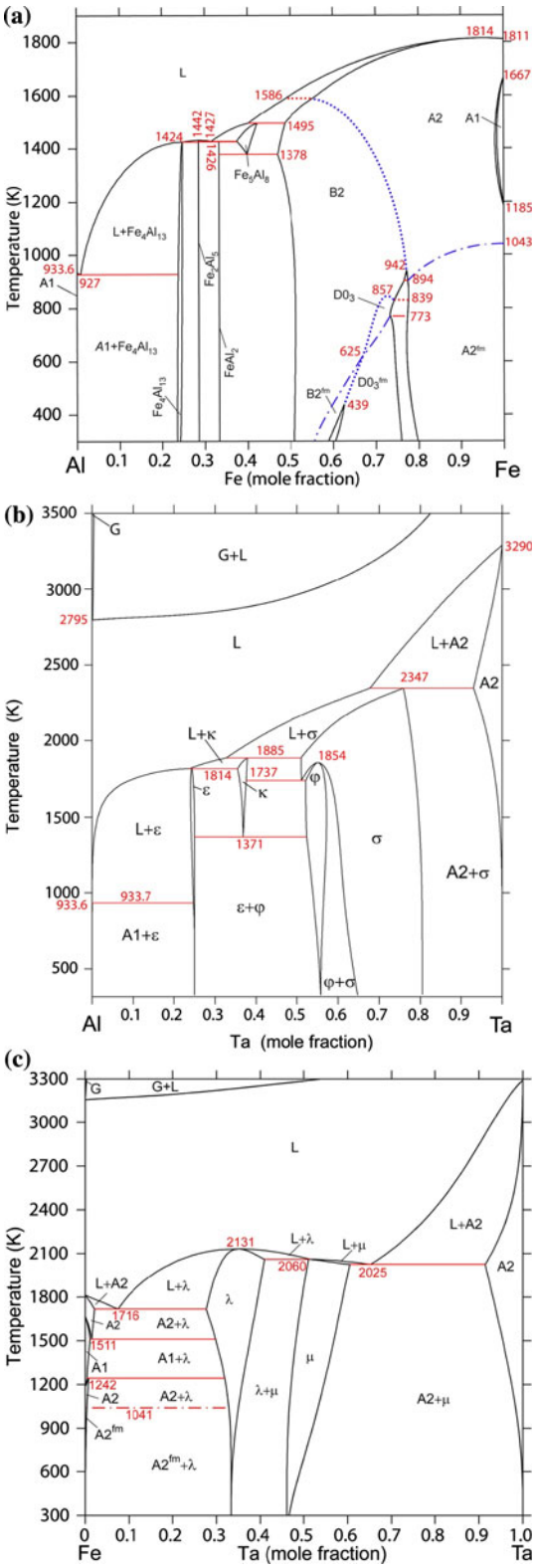

Fig. 11 Phase diagrams of the constituent binary systems Al–Fe (**a**), Al–Ta (**b**) and Fe–Ta (**c**) calculated by means of the thermodynamic descriptions proposed in Refs. [11], [12] and [13], respectively. *Solid lines* denote first-order transformations, *dotted lines* show second-order chemical and *dash-dotted lines* show second-order magnetic transformations

ordering, a 'M' is added; and finally for mixed ordering, 'C-M' are added, as discussed and proposed in [40]. The reaction scheme also outlines 8 isothermal events that mark a change of character of a univariant reaction from first- to second-order or vice versa (tricritical lines)[3] These events are labelled S/F_1, S/F_2,…through S/F_7 and F/S_1, respectively. Six of them correspond to chemical ordering and two to magnetic ordering. The most high temperature tricritical line S/F_1 occurs at 1583 K and corresponds to the change of A2–B2 ordering in the presence of liquid from the second-order univariant equilibrium L + A2/B2 to the first-order univariant equilibrium L + A2 + B2. The only univariant ordering transformation that retains its second-order nature down to room temperature is the B2–$B2^{fm}$ magnetic ordering in the presence of $L2_1^{fm}$.

Owing to the limited experimental data, the ternary ordered Heusler $L2_1$ phase was modelled as a stable phase taking into account trends from experimental information for the ternary systems Al–Fe–Ti [50] and Al–Co–Nb [51]. In these systems, the homogeneity range of the $L2_1$ phase almost reaches the equiatomic FeAl and CoAl composition. Under these assumptions, modelling reveals that the $L2_1$ phase starts to form through a second-order ordering process from the B2 phase of composition $Ta_{0.04}Fe_{0.50}Al_{0.46}$ according to an invariant reaction B2 $\leftrightarrows$ $L2_1 + \lambda$ of eutectoid type at 1122 K (e_{C1}) [40]. With decreasing temperature, the composition of the $L2_1$ phase shifts towards the $TaFe_2Al$ stoichiometry as a result of substitution of Al sites by Ta atoms. At ambient temperature, the $TaFe_2Al$ stoichiometry is reached. The $L2_1$ phase turns out to participate in equilibria with the Fe_3Al-based composition as reported in [6, 7, 9], including the ordered $D0_3$ and $D0_3^{fm}$ forms. Further investigations are, however, needed to understand the thermodynamic stability of the Heusler and Laves phases, as well as the competitive kinetics of their precipitation: the time–temperature diagram presented in [23, 24] suggests that $L2_1$ precipitates are metastable and start to dissolve in favour of Laves phase formation at all temperatures from 923 to 1073 K after sufficient annealing time, e.g. 2000 and 10 h, respectively.

Liquidus and solidus surfaces

The calculated liquidus surface is displayed in Fig. 13a, b as projection on the Gibbs triangle, along with experimentally observed primary phases and with calculated isotherms, respectively. All invariant four-phase reactions involving the liquid phase are marked as in the reaction

[3] The continuous transformations are characterized by singularities in the thermodynamic functions that in phase diagrams occur at critical points or along critical lines or surfaces [40, 44].

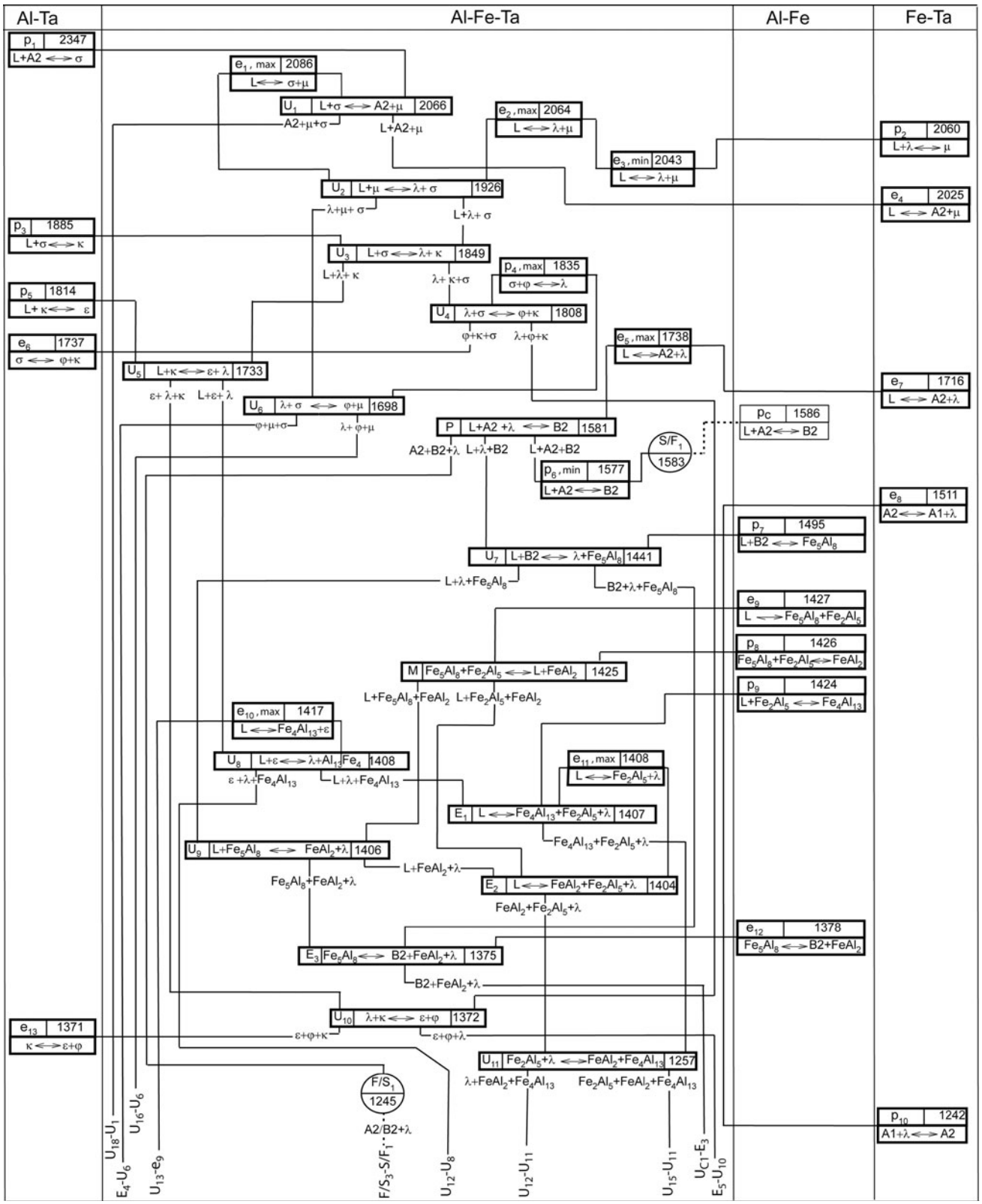

Fig. 12 Reaction scheme down to room temperature for the Al–Fe–Ta system calculated by means of the present thermodynamic description: *solid lines* denote first-order transformations, *dotted lines* show second-order chemical and *dash-dotted lines* show second-order magnetic transformations. The labelling of both, univariant and invariant reactions, is given above

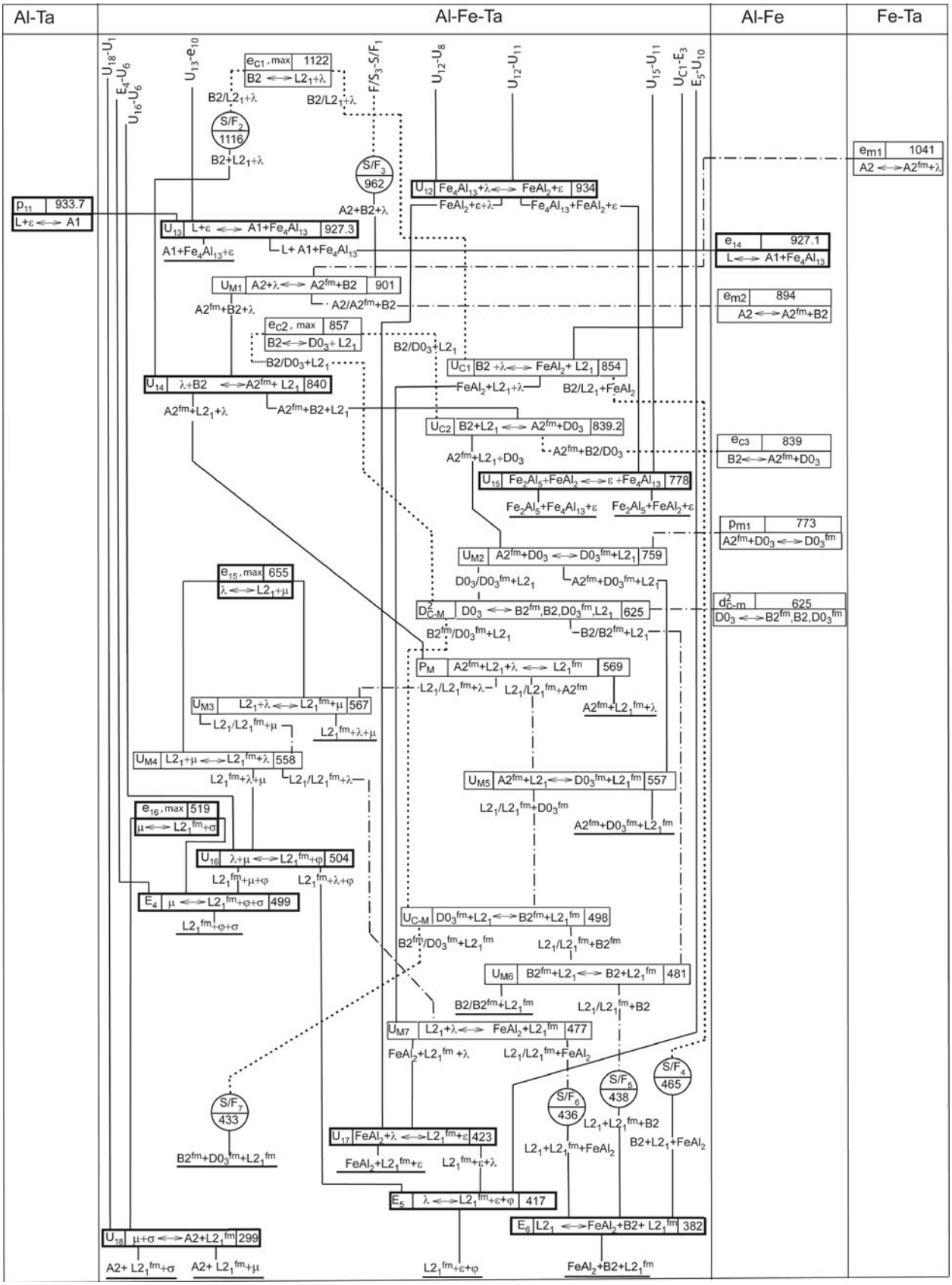

Fig. 12 continued

Table 5 Calculated invariant reactions in the Al–Fe–Ta system involving the liquid phase

Invariant equilibrium $L + \phi_1 + \phi_2 + \phi_3$	Type	T, K	Composition of phases, at.%							
			L		ϕ_1		ϕ_2		ϕ_3	
			Al	Ta	Al	Ta	Al	Ta	Al	Ta
$L \leftrightarrows \lambda$	C_1	2123	29.0	30.5	29.0	30.5	–	–	–	–
$L \leftrightarrows \mu$	C_2	2095	22.0	52.0	22.0	52.0	–	–	–	–
$L \leftrightarrows \mu + \sigma$	e_1	2086	22.3	56.8	23.1	53.6	17.9	74.1	–	–
$L + \sigma \leftrightarrows A2 + \mu$	U_1	2066	10.9	62.4	10.2	78.2	3.7	88.4	13.1	56.7
$L \leftrightarrows \lambda + \mu$	e_2	2064	25.6	42.4	28.7	32.2	23.2	50.0	–	–
$L \leftrightarrows \lambda + \mu$	e_3	2043	7.6	43.6	8.7	32.2	6.7	51.2	–	–
$L + \mu \leftrightarrows \lambda + \sigma$	U_2	1926	51.7	37.7	39.5	47.6	48.5	32.6	42.3	56.4
$L + \sigma \leftrightarrows \kappa + \lambda$	U_3	1849	61.2	31.6	47.2	52.4	58.5	38.1	53.5	32.5
$L \leftrightarrows A2 + \lambda$	e_5	1738	9.6	6.4	9.9	2.6	7.9	25.9	–	–
$L + \kappa \leftrightarrows \varepsilon + \lambda$	U_5	1733	71.9	18.6	62.7	35.7	75.2	23.9	56.0	31.8
$L + A2 + \lambda \leftrightarrows B2$	P	1581	46.1	4.7	41.7	2.4	33.1	28.8	42.1	3.1
$L + A2 \leftrightarrows B2$	p_6	1577	49.2	2.6	43.7	1.3	44.1	1.4	–	–
$L + B2 \leftrightarrows Fe_5Al_8 + \lambda$	U_7	1441	59.9	3.8	50.8	1.5	59.1	0.8	42.9	29.9
$Fe_5Al_8 + Fe_2Al_5 \leftrightarrows L + FeAl_2$	M	1425	62.5	8×10^{-2}	71.4	2×10^{-2}	68.3	0.1	66.6	2×10^{-2}
$L \leftrightarrows Fe_4Al_{13} + \varepsilon$	e_{10}	1417	74.4	2.6	74.3	1.1	75.1	22.8	–	–
$L + \varepsilon \leftrightarrows Fe_4Al_{13} + \lambda$	U_8	1408	69.2	4.1	75.0	22.9	73.7	1.9	49.9	30.4
$L \leftrightarrows Fe_2Al_5 + \lambda$	e_{11}	1408	68.5	3.9	71.0	0.2	48.4	30.1	–	–
$L \leftrightarrows Fe_4Al_{13} + Fe_2Al_5 + \lambda$	E_1	1407	69.1	4.1	73.7	1.9	71.2	0.3	49.9	30.4
$L + Fe_5Al_8 \leftrightarrows FeAl_2 + \lambda$	U_9	1406	64.8	3.8	61.7	1.0	66.4	0.2	46.7	30.2
$L \leftrightarrows Fe_2Al_5 + FeAl_2 + \lambda$	E_2	1404	65.9	3.8	71.1	0.3	66.5	0.2	47.4	30.2
$L + \varepsilon \leftrightarrows A1 + Fe_4Al_{13}$	U_{13}	927.3	99.1	4×10^{-3}	75.2	24.5	99.9	4×10^{-2}	76.1	0.2

scheme (see Fig. 12). The primary λ and μ fields are quite extended towards the Al–Ta side and cover a major part of the liquidus surface. Measured values of the chemical compositions of two-phase eutectics (see data for as-cast samples no. 3, 4, 7–10 and 19 in Table 2) are in proper accordance with the calculated univariant lines (see Fig. 13a). The $L \leftrightarrows \mu + \sigma$ and $L \leftrightarrows A2 + \lambda$ univariant reaction lines display temperature maxima at points e_1 and e_5, corresponding to the quasi-binary eutectics. This agrees well with the results of DTA, described in 'DTA and DSC analysis of transformation temperatures' section. The position of the quasi-binary reaction e_5 is similar to the one reported for the Al–Fe–Nb system [52]. The calculations revealed more complex variation of the liquidus univariant $L + \lambda + \mu$ line in the composition range (5–27)Al–(50-30)Fe–(42–44)Ta (at.%): it changes its character from peritectic $L + \lambda \leftrightarrows \mu$ to eutectic $L \leftrightarrows \mu + \lambda$ with increasing Al content and then passes through two points corresponding to invariant quasibinary reactions (e_3 and e_2, respectively) with temperature difference of 21 K (see Table 5). Such behaviour of the univariant $L - \lambda - \mu$ groove is related to the presence of two congruent equilibria between liquid and λ at $T = 2123$ K (29Al–40.5Fe–30.5Ta) and liquid and μ at $T = 2095$ K (22Al–26Fe–52Ta) marked as 'C_1' and 'C_2' in Fig. 13b, respectively.

The calculated solidus surface is shown in Fig. 14a as projection on the Gibbs triangle along with experimental data on single-phase domains and tie-lines. The calculated solidus surface in Fig. 14b includes calculated isotherms. The solidus surface contains 12 tie-triangles corresponding to the four-phase invariant reactions with the liquid phase, as described above. In total, 7 folds are marked by thick solid lines, corresponding to the quasi-binary invariant reactions with the liquid phase. The solidus surface also shows the wide homogeneity range for the phases λ, μ and σ that extend to 56 at.% Al, 39 at.% Al and 12 at.% Fe, respectively. This is in proper agreement with the XRD and EDS measurements described in 'SM/EDS analysis of samples' and 'XRD analysis of samples' sections.

Isothermal sections

Figures 15, 16 and 17 display a series of calculated isothermal sections: experimentally measured tie-lines and tie-triangles from literature [23, 24] and from the present study are included. For $T = 1973$ K (Fig. 15a) and

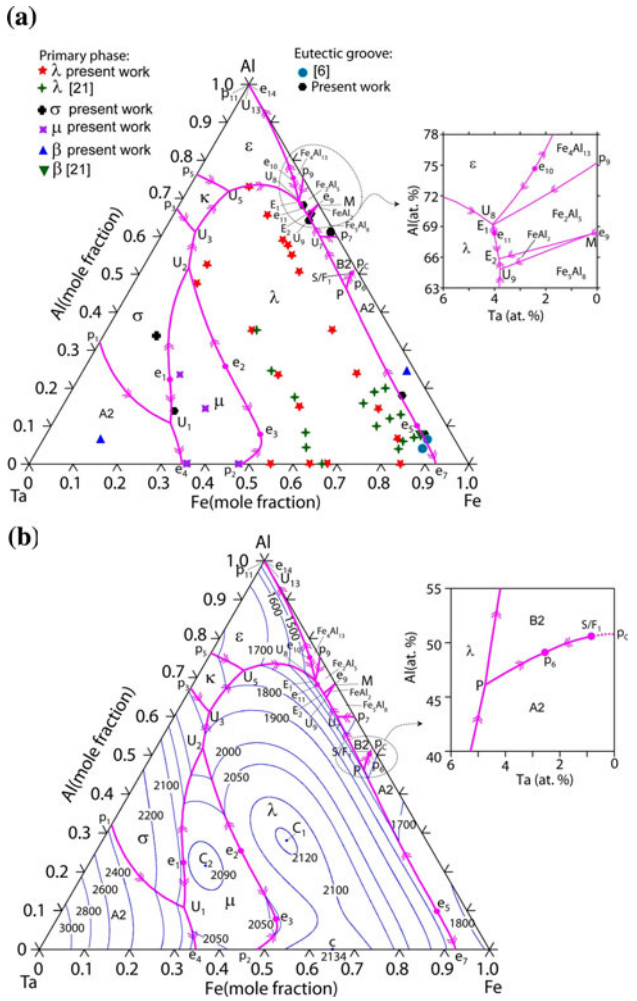

Fig. 13 (Colour online). Calculated liquidus projection for the Al–Fe–Ta system with experimentally observed primary solidification phases reported in [6, 21] and identified in the present study (**a**) and liquidus projection with isotherms (**b**)

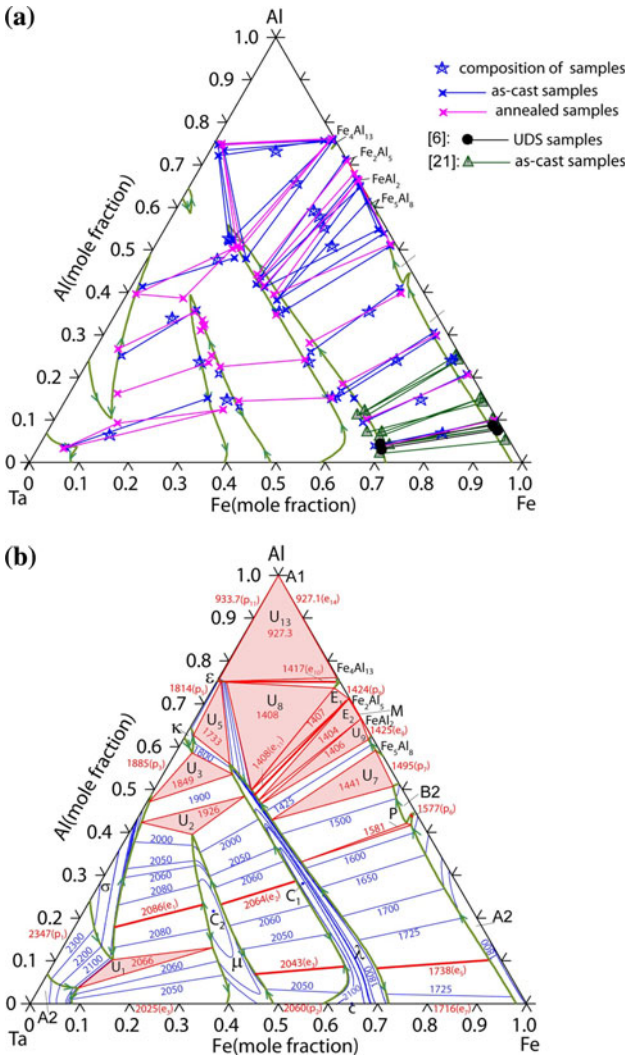

Fig. 14 (Colour online). Calculated compositions of single phases at solidus temperature for the Al–Fe–Ta system compared with measured data in [6, 21] and the present study (**a**) and calculated solidus projection of the system with isotherms (**b**)

$T = 1723$ K (Fig. 15b), tie-lines data stem from the present study only. For $T = 1723$ K, the tie-line between A2 and liquid was determined at a planar interface quenched in after unidirectional solidification of the alloy no. 20. The isothermal sections for $T = 1423$ K (Fig. 15c), $T = 1273$ K (Fig. 15d) and $T = 1073$ K (Fig. 15f) contain the tie-lines reported in [23, 24] for samples annealed for 100, 200 and 1000 h, respectively. The isothermal section for $T = 1123$ K (Fig. 15e) contains the tie-lines experimentally measured in samples no. 1, 2, 3, 8 and 15 annealed for 744 h followed by quenching in water. The directions of all experimental and calculated tie-lines are markedly different, while the phase boundaries are reasonably matched. Our attempts to better reproduce the experimental tie-line directions always led to unacceptable distortions of the phase boundaries, especially for A2 and B2, and were therefore abandoned. It is likely that the experimental tie-lines do not correspond to phase equilibrium, meaning that annealed samples still contain residual micro-segregation inherited from solidification and longer annealing may be required to equilibrate them.

Calculated isothermal sections for $T = 873$, 573, 500 and 298 K are displayed in Fig. 16a–d, showing the occurrence of ordered $D0_3$ and Heusler $L2_1$ phases, as well as three-phases fields $A2^{fm} + D0_3^{fm} + L2_1^{fm}$ and $B2^{fm} + D0_3^{fm} + L2_1^{fm}$ that arise from first-order chemical and magnetic transformations. The univariant phase equilibria with ordered and disordered phases are also outlined by dotted lines for chemical ordering and dash-dotted lines for magnetic ordering. Experimental data for these low temperatures are scarce, comprising only DTA and DSC measurements of the present study and from [7, 23–25], and further experimental studies are required. Figure 16c shows that the Heusler $L2_1$ phase approaches the $TaFe_2Al$ stoichiometry and both the λ and μ phase fields are

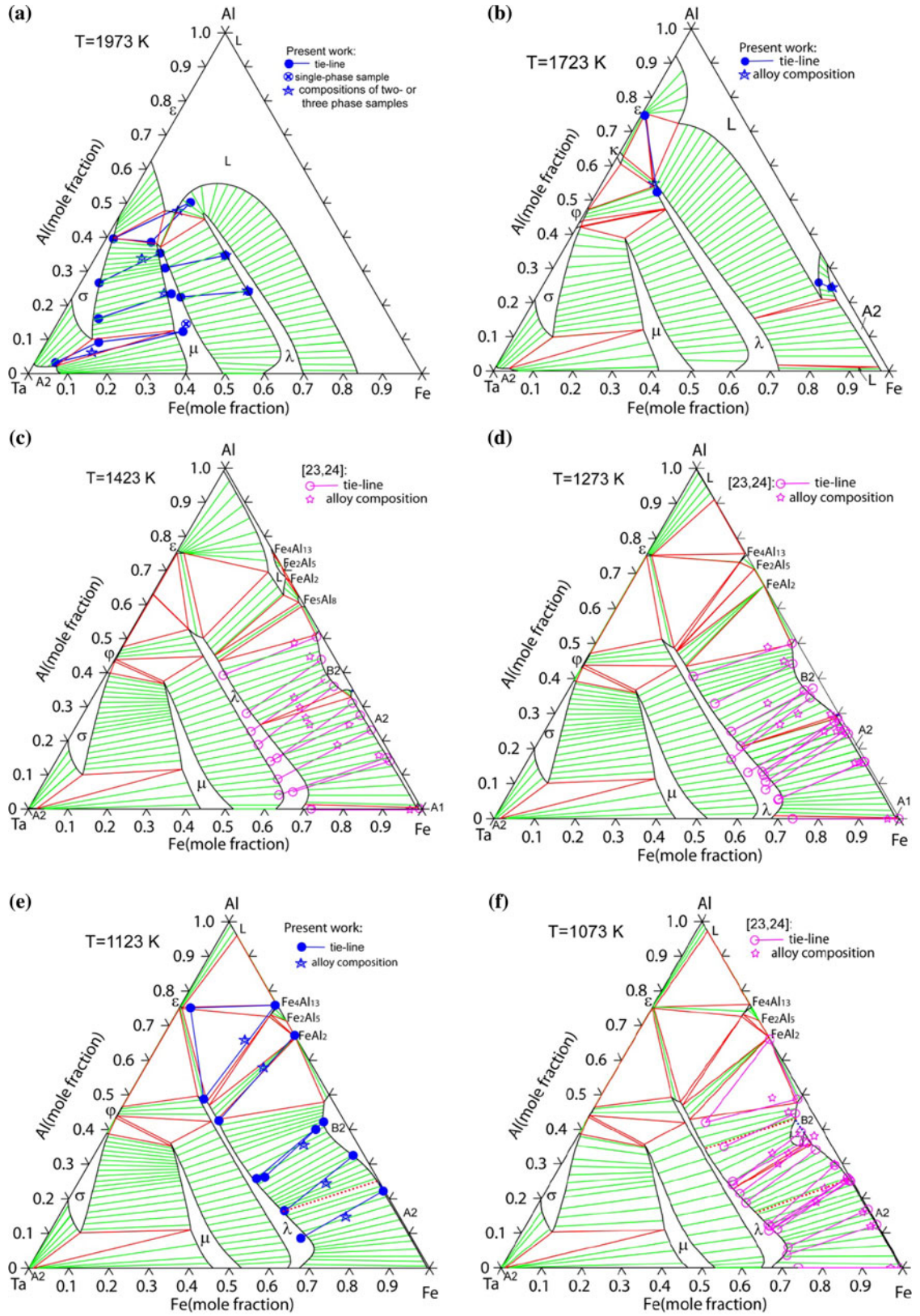

Fig. 15 (Colour online). Isothermal sections for the Al–Fe–Ta system at $T = 1973$ K (**a**), $T = 1723$ K (**b**), $T = 1423$ K (**c**), $T = 1273$ K (**d**), $T = 1123$ K (**e**) and $T = 1073$ K (**f**). *Lines* are calculated phase equilibria by means of the proposed thermodynamic description and *tie-lines* and *tie-triangles* assigned by *symbols* are experimental data from the present study and from [23, 24]. *Dotted lines* separate ordered from disordered phases (chemical ordering)

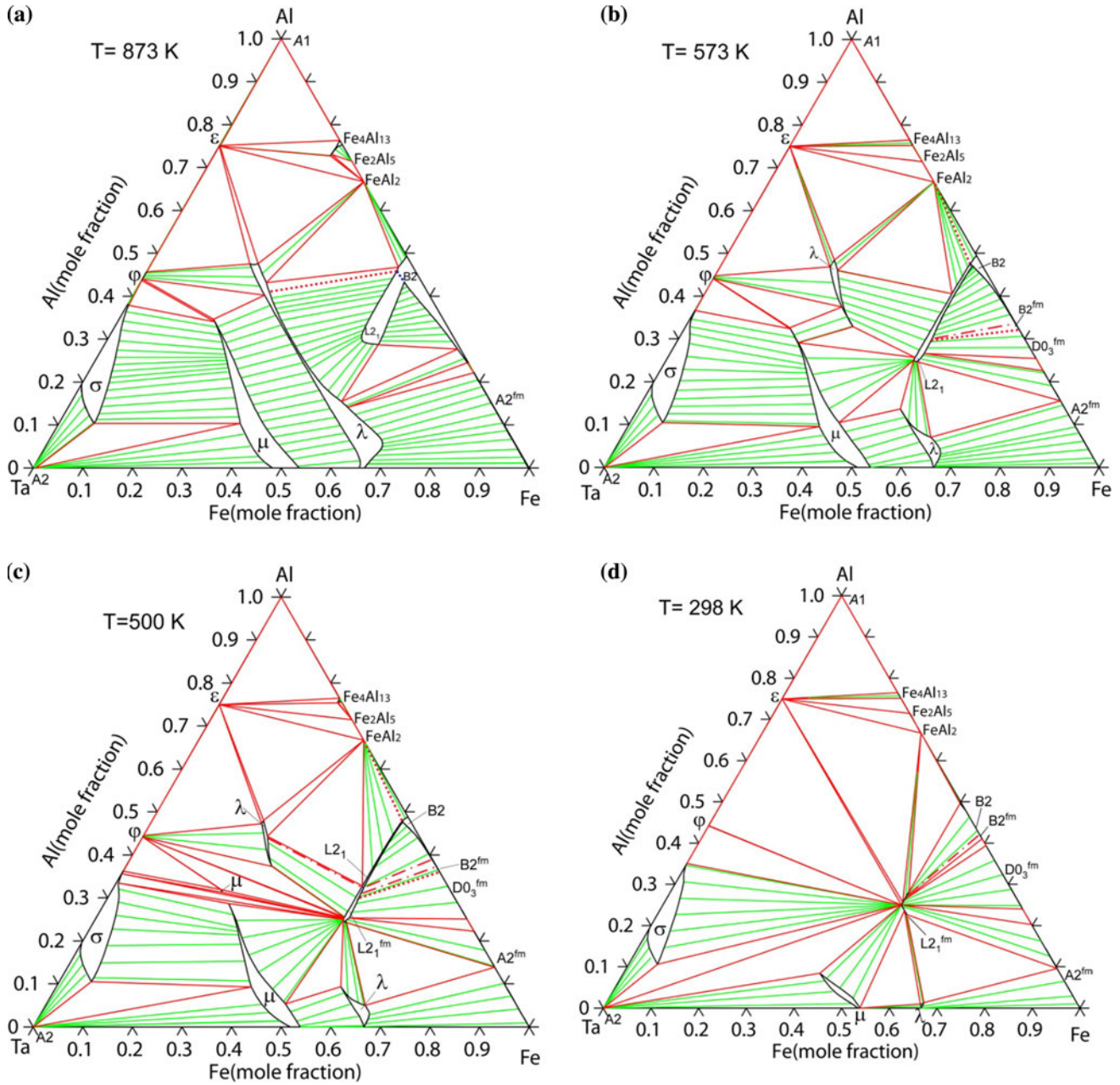

Fig. 16 (Colour online). Calculated isothermal sections for the Al–Fe–Ta system at moderate and ambient temperatures $T = 873$ K (**a**), $T = 573$ K (**b**), $T = 500$ K (**c**) and $T = 298$ K (**d**). *Dotted lines* separate ordered from disordered phases (chemical ordering) and *dash-dotted lines* separate the paramagnetic from the ferromagnetic state of A2, B2, $D0_3$ and $L2_1$

present as two islands. Such feature was reported in [7, 14, 20], but for a temperature value of 1273 K. Finally, Fig. 16d shows the calculated isothermal section at room temperature: the ferromagnetic Heusler phase $L2_1^{fm}$ appears as a ternary line compound with the composition quite close to the $TaFe_2Al$ stoichiometry, being the dominant phase in the entire system. Only one three-phase field $B2/B2^{fm} + L2_1^{fm}$ associated with second-order magnetic transformation remains present at this temperature (see also reaction scheme in Fig. 12), which is shown by dash-dotted line.

Isopleths

Selected isopleths are presented in Figs. 17 and 18, aiming to compare calculated phase transformation temperatures with experimental data from literature, from DTA and DSC measurements reported in 'DTA and DSC analysis of transformation temperatures' section. The experimental data points are not always precisely in the plane of the calculated isopleths, but may deviate by maximum 2 at.%. Figure 17b also illustrates the reproducibility of DTA

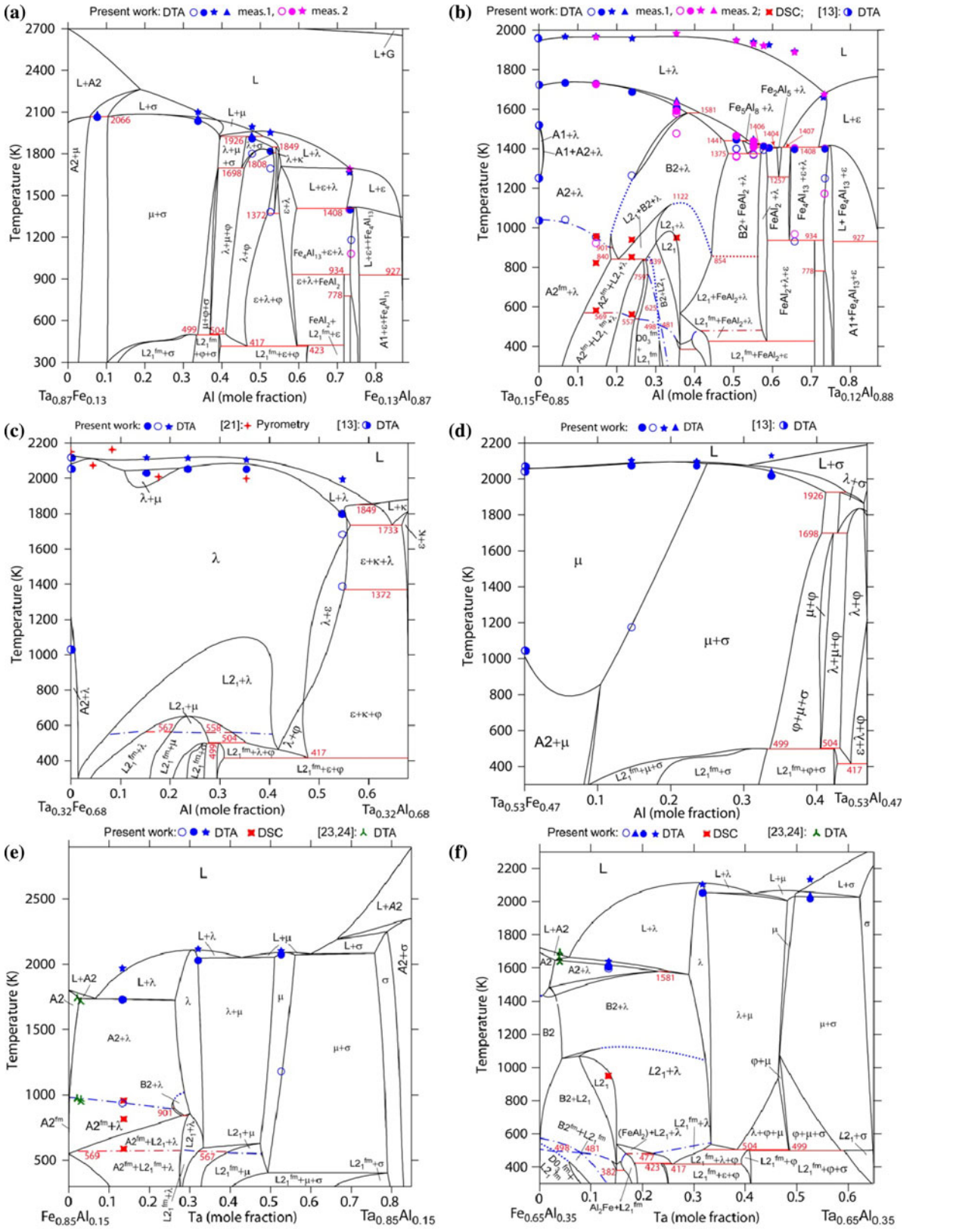

Fig. 17 (Colour online). Calculated isopleths for the Al–Fe–Ta system (*lines*) compared to experimentally determined phase transformation temperatures reported in [13, 21, 23, 24] and in 'DTA and DSC analysis of transformation temperatures' section of the present study for 13 at.% Fe (**a**), $Ta_{15}Fe_{85}$–$Ta_{12}Al_{88}$ (**b**), 32 at.% Ta (**c**), 53 at.% Ta (**d**), 15 at.% Al (**e**) and 35 at.% Al (**f**). *Dotted lines* show chemical ordering and *dash-dotted lines* show magnetic ordering accomplished by second-order transformations

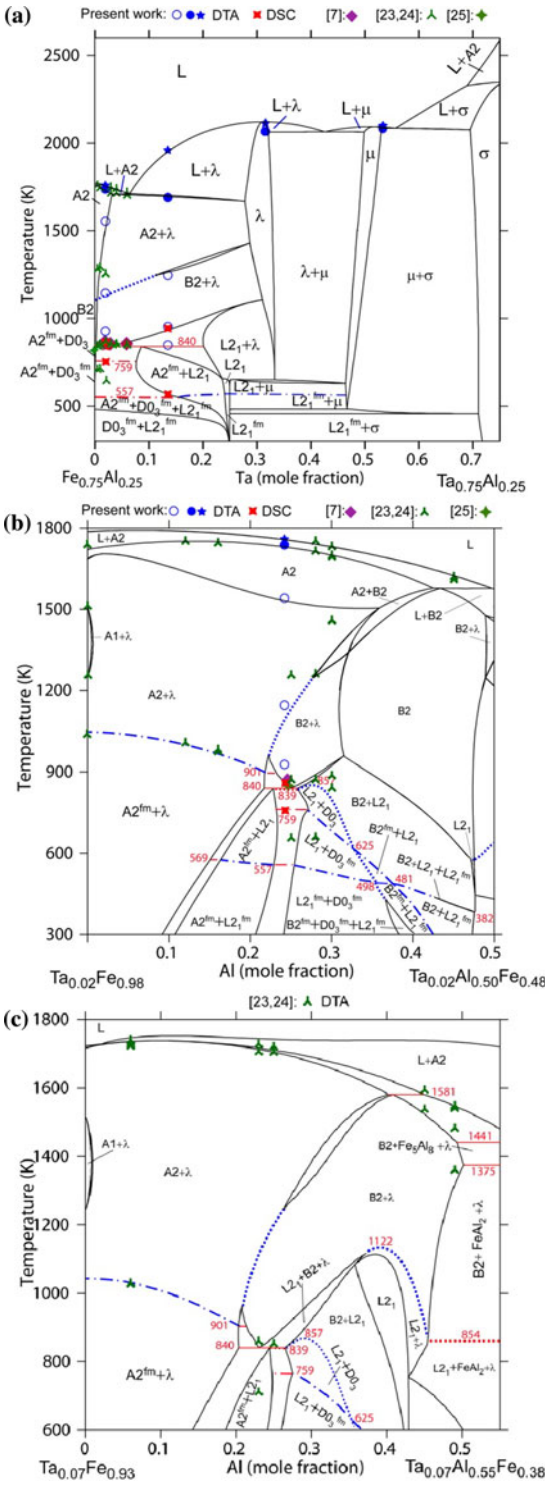

Fig. 18 (Colour online). Calculated isopleths for the Al–Fe–Ta system at 25 at.% Al (**a**), 2 at.% Ta (**b**) and 7 at.% Ta (**c**) along with experimentally determined phase transformation temperatures reported 'DTA and DSC analysis of transformation temperatures' section and published in [7, 23–25]. *Dotted lines* show chemical ordering and *dash-dotted lines* show magnetic ordering accomplished by second-order transformations

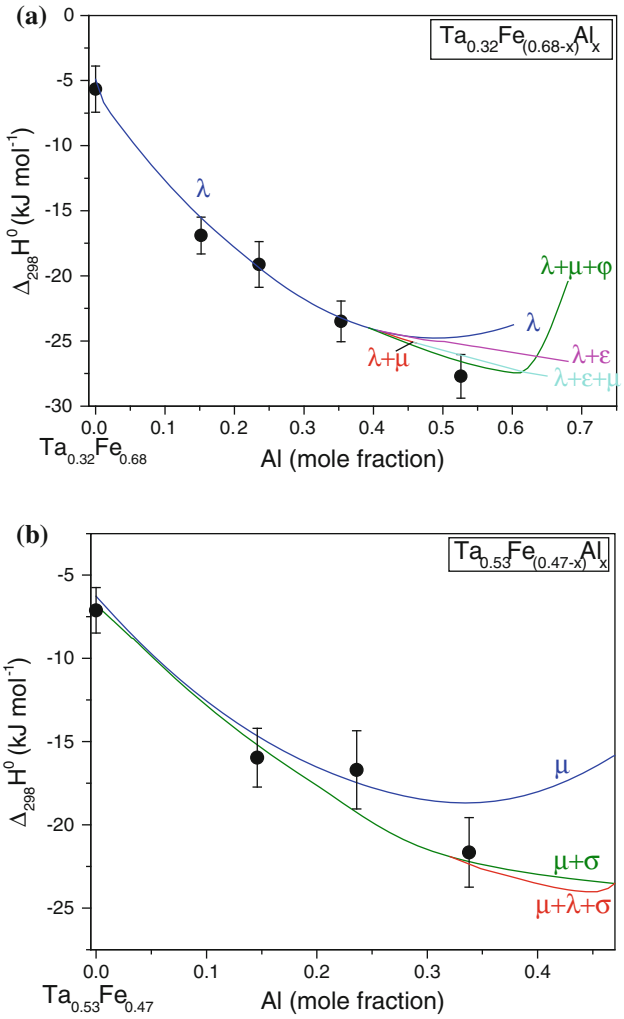

Fig. 19 (Colour online). Standard enthalpies of formation of Al–Fe–Ta alloys having the λ (**a**) or the μ (**b**) phase as single or major microstructure constituent. *Symbols* are experimental data reported in 'Dissolution calorimetry' section, while lines are calculated values by the present thermodynamic description for $Ta_{0.32}Fe_{0.68-x}Al_x$ and $Ta_{0.53}Fe_{0.47-x}Al_x$ isoconcentration sections. The reference state is fcc-Al, bcc-Fe and bcc-Ta at 298.15 K

signals for several alloys in the annealed condition obtained in two distinct runs performed at heating and cooling rates of 20 K min^{-1}. The calculated phase transformation temperatures agree with experimentally measured values of the present study, except for the liquidus temperatures of the alloys no. 6, 7, 8 (Fig. 17b) and no. 11 (Fig. 17c). These Al-rich alloys are believed to suffer partly from considerable loss of Al by evaporation when heating the liquid above 1800 K. A further contribution to the observed differences between measured and calculated liquidus temperatures of the Al-rich samples no. 6–8 may relate to a slower kinetics of dissolution (retarded dissolution) of the Al-rich ternary Laves phase, as may be

suspected from its high negative enthalpy of formation (Fig. 19a) and refractoriness (see Fig. 14b).

The melting temperatures of λ reported by Von Keitz et al. [21] (Fig. 17c), as well as the recent DTA results of Risanti and Sauthoff [7, 23, 24] (Fig. 18), are also reasonably reproduced. In numerous alloys, the temperature associated to A2–B2, B2–$L2_1$ and A2–$A2^{fm}$ second-order transformations was clearly detected on the DTA curves, and these data agree well with the calculations (see dotted and dash-dotted lines in Figs. 17a, e, f, 18a, b).

The alloy no. 20 ($Ta_{2.0}Fe_{73.5}Al_{24.3}C_{0.2}$) as attractive for industry received much attention, aiming to understand precipitation and ordering at potential service temperatures below 900 K. The isopleths displayed in Fig. 18a, b show that below 839 K, this alloy should be composed of $A2^{fm} + D0_3 + L2_1$ and above 860 K of B2 and λ-phase. The disordering transformations upon heating should occur through a second-order invariant reaction $A2^{fm} + D0_3 \rightarrow B2 + L2_1$ at 839 K (U_{C2}) followed by a first-order invariant reaction $A2^{fm} + L2_1 \rightarrow B2 + \lambda$ at 840 K (U_{14}) and should finish after passing through $A2^{fm} + B2 + \lambda \backslash B2 + \lambda$ phase boundary at 860 K. We attempted to verify these transformations by DSC and XRD techniques; however, the complex reaction sequence requires more detailed analysis in future. At this stage, we can only emphasise that the precipitates formed upon annealing at 923 and 1123 K are Laves phase; whereas, after the annealing at 823 K for 362 h, only the nanosized Heusler phase precipitates in A2(Fe) matrix were identified (see Figs. 4, 6), which are in accordance with the thermodynamic calculations.

Thermodynamic properties

Figure 19 displays experimentally measured values of the standard enthalpy of formation of ternary Al–Fe–Ta alloys containing the λ and μ phases as a major microstructure constituent. The calculated standard enthalpy of formation is equally shown as a function of the aluminium content, i.e. for the $Ta_{0.32}Fe_{(0.68-x)}Al_x$ and $Ta_{0.53}Fe_{(0.47-x)}Al_x$ isoconcentration sections. Both measured and calculated data refer to fcc-Al, bcc-Fe, bcc-Ta at 298.15 K and to identical formula units. Because samples of both series, excluding alloy no. 18 (see Table 2), were not single-phased materials, calculations were performed that comprise both the major phase and its mixtures with potential minor phase constituents. The calculated and measured values agree well to one another for both series of alloys being inside or close to the homogeneity ranges of λ and μ phases. The results show that λ and μ become more stable after dissolution of about 50 and 33 at.% Al, respectively. This is the main reason for their considerable extension into the ternary Al–Fe–Ta system and also explains the existence of C_1 and C_2 points of their congruent melting/solidification, as well as e_1, e_2 and e_4 maxima in the $L + \mu + \sigma$, $L + \lambda + \mu$ and $L + A2 + \lambda$ univariant liquidus lines, respectively (see Figs. 12, 13b).

Summary and conclusions

Based on the literature data and selected key experiments, a new thermodynamic description of the ternary Al–Fe–Ta system has been proposed. The study encompassed

- experimental analysis of 20 distinct alloys in both as-cast and annealed states by XRD, SEM/EDS, DTA and DSC techniques for the analysis of microstructure constituents, composition of coexisting phases and phase transition temperatures;
- determination of the standard enthalpies of formation of λ and μ ternary phases by means of isoperibolic dissolution calorimetry;
- thermodynamic modelling by the CALPHAD method, taking into account assessed experimental information from literature and our own experimental results;
- formulation of the complete reaction scheme, comprising first-order reactions, as well as chemical and magnetic ordering transformations of second-order nature;
- thermodynamic calculations of liquidus and solidus surfaces, selected isothermal and vertical sections, and the standard enthalpy of formation of solid alloys in comparison to experimental data.

The investigations lead to the following conclusions: the ternary alloy system Al–Fe–Ta is the host to several intermetallic phases with extended homogeneity ranges (i) the C14 Laves phase λ based on $TaFe_2$ can dissolve up to 56 at.% Al, (ii) the $D8_5$ μ phase can dissolve up to 39 at.% Al, (iii) the σ phase based on Ta_2Al can dissolve up to 12 at.% Fe and finally (iv) the ternary Heusler $L2_1$ phase presumably forms in the course of a second-order ordering reaction $B2 \rightarrow L2_1 + \lambda$ of eutectoid type at 1122 K in the vicinity of $Ta_{0.04}Fe_{0.50}Al_{0.46}$ and shifts with decreasing temperature towards the ideal $TaFe_2Al$ stoichiometry.

The proposed CALPHAD description can reproduce major part of experimental data on phase equilibria. It also yields reliable values for the standard enthalpy of formation of solid Al–Fe–Ta phases. The complete database attached will serve as a guide for other scientists to operate with Al–Fe–Ta materials and design their future experiments or even improve the description and clarify still open questions related to the formation of the Heusler phase.

Acknowledgments The authors thank L. A. Duma, V. V. Garbuz, V. A. Petrova and A. Genau for technical assistance, and would like to express their gratitude for the financial support from the German Federal Ministry of Research (Contract FKZ 50WM0843) and the National Academy of Science of Ukraine (Project III-6-10: 0110U002347).

Appendix

Thermodynamic database of Al–Fe–Ta system in Thermo-Calc format.

```
 ELEMENT VA  VACUUM           0.0000E+00  0.0000E+00  0.0000E+00 !
 ELEMENT AL  A1_FCC           2.6982E+01  4.5773E+03  2.8322E+01 !
 ELEMENT FE  A2_BCC           5.5847E+01  4.4890E+03  2.7280E+01 !
 ELEMENT TA  A2_BCC           1.8095E+02  5.6819E+03  4.1472E+01 !
 SPECIES AL2              AL2 !
 SPECIES FE2              FE2 !

FUNC ALGAS     298.15  +308413.104-26.8663217*T-20.78039*T*LN(T)
   +3.520865E-08*T**2-1.789015E-10*T**3-27114.25*T**(-1);  3.30000E+03  Y
    +294502.846+22.5173774*T-26.85062*T*LN(T)+.001194919*T**2
   -4.501805E-08*T**3+6025110*T**(-1);  6.40000E+03  Y
    +447945.062-285.801392*T+8.243415*T*LN(T)-.0023944315*T**2
   +2.426725E-08*T**3-1.2048605E+08*T**(-1);  9.40000E+03  Y
    +349945.955-150.289475*T-6.454579*T*LN(T)-.0014339715*T**2
   +1.278805E-08*T**3;  1.00000E+04  N !
FUNC AL2GAS     298.15  +480383.542-1.58706566*T-36.90579*T*LN(T)
   -7.56815E-04*T**2-1.31040183E-07*T**3+16498.85*T**(-1);  1.60000E+03  Y
    +484703.82-58.8210679*T-28.53999*T*LN(T)-.00618347*T**2
   +4.55704333E-07*T**3;  3.10000E+03  Y
    +399551.917+333.52963*T-78.48514*T*LN(T)+.006619755*T**2
   -1.5106045E-07*T**3+26673440*T**(-1);  3.80000E+03  N !
FUNC FEGAS     298.15  +401732.827+37.9381886*T-32.861*T*LN(T)
   +.00908265*T**2-1.34845667E-06*T**3+108791.4*T**(-1);  9.00000E+02  Y
    +410335.744-51.7107058*T-19.84276*T*LN(T)+6.959445E-05*T**2
   -1.30682983E-07*T**3-976411.5*T**(-1);  2.40000E+03  Y
    +406591.004-47.1975307*T-20.12513*T*LN(T)-5.66549E-04*T**2
   -5.290265E-08*T**3+887592*T**(-1);  5.50000E+03  Y
    +518056.742-373.01803*T+18.70844*T*LN(T)-.00634452*T**2
   +1.038655E-07*T**3-55487750*T**(-1);  1.00000E+04  N !
FUNC FE2GAS     298.15  +496936.137+167.757207*T-48.04721*T*LN(T)
   +.0045131445*T**2-1.38132583E-06*T**3+1236257.5*T**(-1);  1.10000E+03  Y
    +413625.937+278.684005*T-57.36458*T*LN(T)+7.8394E-05*T**2
   +3.40843667E-07*T**3+40989960.5*T**(-1);  2.50000E+03  Y
    +457326.556+298.173624*T-62.41141*T*LN(T)+.00532538*T**2
   -1.30827917E-07*T**3-6839750*T**(-1);  6000  N !
FUNC TAGAS     298.15  +778354.148-86.9745131*T-14.20039*T*LN(T)
   -.007338225*T**2+1.78913E-07*T**3-105967.1*T**(-1);  7.00000E+02  Y
    +777752.285-88.0986009*T-13.78268*T*LN(T)-.00918088*T**2
   +7.334755E-07*T**3+24159.195*T**(-1);  1.60000E+03  Y
    +754463.426+77.8713183*T-36.40211*T*LN(T)+6.75171E-04*T**2
   -7.82934667E-08*T**3+4567559*T**(-1);  5.10000E+03  Y
    +895631.819-338.928535*T+13.40182*T*LN(T)-.0069422*T**2
   +1.36139367E-07*T**3-67869550*T**(-1);  8.40000E+03  Y
    +322438.534+636.08615*T-95.23214*T*LN(T)+.0022289675*T**2
   -9.27389167E-09*T**3+5.00859E+08*T**(-1);  1.00000E+04  N !
FUNC GHSERAL   2.98140E+02  -7976.15+137.093038*T-24.3671976*T*LN(T)
   -.001884662*T**2-8.77664E-07*T**3+74092*T**(-1);  7.00000E+02  Y
    -11276.24+223.048446*T-38.5844296*T*LN(T)+.018531982*T**2
   -5.764227E-06*T**3+74092*T**(-1);  9.33470E+02  Y
    -11278.378+188.684153*T-31.748192*T*LN(T)-1.230524E+28*T**(-9); 2.90000E+03  N !
FUNC GFCCFE    298.15  -236.7+132.416*T-24.6643*T*LN(T)
   -.00375752*T**2-5.8927E-08*T**3+77359*T**(-1);  1.81100E+03  Y
    -27097.396+300.25256*T-46*T*LN(T)+2.78854E+31*T**(-9); 6000  N !
FUNC GHSERTA   2.98140E+02  -7285.889+119.139858*T-23.7592624*T*LN(T)
   -.002623033*T**2+1.70109E-07*T**3-3293*T**(-1);  1.30000E+03  Y
    -22389.955+243.88676*T-41.137088*T*LN(T)+.006167572*T**2
```

```
    -6.55136E-07*T**3+2429586*T**(-1);  2.50000E+03  Y
     +229382.886-722.59722*T+78.5244752*T*LN(T)-.017983376*T**2
    +1.95033E-07*T**3-93813648*T**(-1);  3.25800E+03  Y
     -963392.734+2773.7774*T-337.227976*T*LN(T)+.039791303*T**2
    -9.74251E-07*T**3+5.09949511E+08*T**(-1);  6000  N !
FUNC GBCCAL    298.15  +10083-4.813*T+GHSERAL#;  6000   N !
FUNC GHSERFE   298.15  +1225.7+124.134*T-23.5143*T*LN(T)
    -.00439752*T**2-5.8927E-08*T**3+77359*T**(-1);  1.81100E+03  Y
     -25383.581+299.31255*T-46*T*LN(T)+2.29603E+31*T**(-9); 6000  N !
FUNC GD03ALFE  298.15  +2*UBALFE1#+UBALFE2#+3900;  6000   N !
FUNC GB2ALFE   298.15  +4*UBALFE1#;  6000   N !
FUNC GLIQAL    298.15  +11005.029-11.841867*T+7.934E-20*T**7+GHSERAL#;  9.33470E+02  Y
    +10482.382-11.253974*T+1.231E+28*T**(-9)+GHSERAL#;  6000  N !
FUNC GLIQFE    298.15  +12040.17-6.55843*T-3.67516E-21*T**7+GHSERFE#;  1.81100E+03  Y
    +14544.751-8.01055*T+GHSERFE#-2.29603E+31*T**(-9);  6000  N !
FUNC GLIQTA    2.98140E+02  +29160.975-7.578729*T+GHSERTA#;  1.00000E+03  Y
    +51170.228-181.121652*T+23.7872147*T*LN(T)-.009707033*T**2
    +4.4449E-07*T**3-3520045*T**(-1)+GHSERTA#;  1.30000E+03  Y
    +66274.294-305.868555*T+41.1650403*T*LN(T)-.018497638*T**2
     +1.269735E-06*T**3-5952924*T**(-1)+GHSERTA#;  2.50000E+03  Y
      -185498.547+660.615425*T-78.4965229*T*LN(T)+.00565331*T**2
     +4.19566E-07*T**3+90290310*T**(-1)+GHSERTA#;  3.29000E+03  Y
      +1036069.47-2727.38037*T+320.319132*T*LN(T)-.043117795*T**2
     +1.055148E-06*T**3-5.54714342E+08*T**(-1)+GHSERTA#;  6000  N !
 FUNC LFALFE0   298.15  -104700+30.65*T;  6000   N !
 FUNC LFALFE1   298.15  +30000-7*T;  6000   N !
 FUNC LFALFE2   298.15  +32200-17*T;  6000   N !
 FUNC ZERO      298.15 0.0; 6000.00  N !
 FUNC GAL3FE    298.15  +3*UFALFE#+9000;  6000   N !
 FUNC GAL2FE2   298.15  +4*UFALFE#;  6000   N !
 FUNC GALFE3    298.15  +3*UFALFE#-3500;  6000   N !
 FUNC SFALFE    298.15  +UFALFE#;  6000   N !
 FUNC GB32ALFE  298.15  +2*UBALFE1#+2*UBALFE2#;  6000   N !
 FUNC GD03FEAL  298.15  +2*UBALFE1#+UBALFE2#-70+.5*T;  6000   N !
 FUNC ORD1      298.15  +18455-3.5*T;  6000   N !
 FUNC UBALFE1   298.15  -4023-1.14*T;  6000   N !
 FUNC UBALFE2   298.15  -1973-2*T;  6000   N !
 FUNC UFALFE    298.15  -4000+T;  6000   N !

 TYPE_DEFINITION % SEQ *!
 DEFINE_SYSTEM_DEFAULT ELEMENT 2 !
 DEFAULT_COMMAND DEF_SYS_ELEMENT VA /- !

 PHASE GAS:G %  1  1.0  !
   CONSTITUENT GAS:G :AL,AL2,FE,FE2,TA :  !
  PAR G(GAS,AL;0),,  +ALGAS#+R#*T*LN(1E-05*P);  6000   N SSUB4 !
  PAR G(GAS,AL2;0),,  +AL2GAS#+R#*T*LN(1E-05*P);  6000   N SSUB4 !
  PAR G(GAS,FE;0),,  +FEGAS#+R#*T*LN(1E-05*P);  6000   N SSUB4 !
  PAR G(GAS,FE2;0),,  +FE2GAS#+R#*T*LN(1E-05*P);  6000   N SSUB4 !
  PAR G(GAS,TA;0),,  +TAGAS#+R#*T*LN(1E-05*P);  6000   N  SSUB4 !

 TYPE_DEFINITION & GES A_P_D A1_FCC MAGNETIC  -3.0    2.80000E-01 !
 PHASE A1_FCC  %&  2 1   1 !
   CONSTITUENT A1_FCC  :AL,FE,TA : VA :  !
  PAR G(A1_FCC,AL:VA;0),,  +GHSERAL#;  6000   N 91Din !
  PAR G(A1_FCC,FE:VA;0),,  +GFCCFE#;  6000   N 91Din !
  PAR TC(A1_FCC,FE:VA;0),,  -201;  6000   N 09Sun !
  PAR BMAGN(A1_FCC,FE:VA;0),,  -2.1;  6000   N 09Sun  !
  PAR G(A1_FCC,AL,FE:VA;0),,  +LFALFE0#;  6000   N 09Sun  !
  PAR G(A1_FCC,AL,FE:VA;1),,  +LFALFE1#;  6000   N 09Sun !
  PAR G(A1_FCC,AL,FE:VA;2),,  +LFALFE2#;  6000   N 09Sun !
  PAR G(A1_FCC,TA:VA;0),,  +16000+1.7*T+GHSERTA#;  6000   N 10Wit  !
  PAR G(A1_FCC,AL,TA:VA;0),,  -125394.8+78.85*T;  6000   N 10Wit  !
  PAR G(A1_FCC,FE,TA:VA;0),,  -30521;  6000   N 11Wit !
  PAR G(A1_FCC,FE,TA:VA;1),,  34925;  6000   N 11Wit !
$ Parameters evaluated in the present work
  PAR G(A1_FCC,AL,FE,TA:VA;0),,  -50000;  6000   N 12Wit !


 TYPE_DEFINITION ' GES A_P_D A2_BCC MAGNETIC  -1.0    4.00000E-01 !
 PHASE A2_BCC  %'  2 1   3 !
   CONSTITUENT A2_BCC  :AL,FE,TA : VA :  !
  PAR G(A2_BCC,AL:VA;0),,  +GBCCAL#;  6000   N 91Din !
  PAR G(A2_BCC,FE:VA;0),,  +GHSERFE#;  6000   N 91Din  !
  PAR G(A2_BCC,TA:VA;0),,  +GHSERTA#;  6000   N 91Din !
```

```
  PAR TC(A2_BCC,FE:VA;0),,  1043;   6000   N 09Sun !
  PAR BMAGN(A2_BCC,FE:VA;0),,  2.22;   6000   N 09Sun !
  PAR G(A2_BCC,AL,FE:VA;0),,  -122960+32*T;   6000  N 09Sun !
  PAR G(A2_BCC,AL,FE:VA;1),,  2945;   6000   N 09Sun !
  PAR TC(A2_BCC,AL,FE:VA;0),,  -438;   6000   N 09Sun !
  PAR TC(A2_BCC,AL,FE:VA;1),,  -1720;   6000   N 09Sun !
  PAR G(A2_BCC,AL,TA:VA;0),,  -578.901;   6000   N 10Wit !
  PAR G(A2_BCC,FE,TA:VA;0),,  +3442+9.429*T;   6000  N 11Wit !
  PAR G(A2_BCC,FE,TA:VA;1),,  -334;   6000   N 11Wit !
  PAR TC(A2_BCC,FE,TA:VA;0),,  600;   6000   N 11Wit !
$ Parameters evaluated in the present work
  PAR G(A2_BCC,AL,FE,TA:VA;0),,  +40650-50*T;  6000   N 12Wit !
  PAR G(A2_BCC,AL,FE,TA:VA;1),,  -6150-50*T;   6000 N 12Wit !
  PAR G(A2_BCC,AL,FE,TA:VA;2),,  -189850-50*T;   6000   N 12Wit !

 PHASE FE4AL13  %  3 .6275   .235   .1375 !
   CONSTITUENT FE4AL13  :AL : FE : AL,TA,VA :  !
  PAR G(FE4AL13,AL:FE:AL;0),,  -30680+7.4*T+.765*GHSERAL#+.235*GHSERFE#; 6000 N 09Sun !
  PAR G(FE4AL13,AL:FE:VA;0),,  -28100+7.4*T+.6275*GHSERAL#+.235*GHSERFE#; 6000 N 09Sun !
$ Parameters evaluated in the present work
  PAR G(FE4AL13,AL:FE:TA;0),, -19000+.6275*GHSERAL#+.235*GHSERFE#+.1375*GHSERTA#; 6000 N 12Wit !
  PAR G(FE4AL13,AL:FE:AL,TA;0),,  -7500-27.2*T+.0205*T**2; 6000 N 12Wit !

 PHASE FEAL2  %  2 2   1 !
   CONSTITUENT FEAL2  :AL,TA : FE :  !
  PAR G(FEAL2,AL:FE;0),,  -104000+23*T+2*GHSERAL#+GHSERFE#; 6000 N 09Sun !
$ Parameters evaluated in the present work
  PAR G(FEAL2,TA:FE;0),,  +15000+2*GHSERTA#+GHSERFE#; 6000   N 12Wit  !

 PHASE FE2AL5  %  2 5   2 !
   CONSTITUENT FE2AL5  :AL,TA : FE :  !
  PAR G(FE2AL5,AL:FE;0),,  -235600+54*T+5*GHSERAL#+2*GHSERFE#; 6000 N 09Sun !
 $ Parameters evaluated in the present work
  PAR G(FE2AL5,TA:FE;0),,  +40000+5*GHSERTA#+2*GHSERFE#; 6000 N 12Wit  !

 PHASE FE5AL8_CI52  %  2 8   5 !
   CONSTITUENT FE5AL8_CI52  :AL,FE,TA : AL,FE,TA :  !
  PAR G(FE5AL8_CI52,AL:AL;0),,  +13*GBCCAL#;   6000 N 09Sun !
  PAR G(FE5AL8_CI52,FE:AL;0),,  +200000+36*T+5*GBCCAL#+8*GHSERFE#; 6000 N 09Sun !
  PAR G(FE5AL8_CI52,AL:FE;0),,  -394000+36*T+8*GBCCAL#+5*GHSERFE#;  6000 N 09Sun !
  PAR G(FE5AL8_CI52,FE:FE;0),,  +13*GHSERFE#+13000; 6000   N 09Sun !
  PAR G(FE5AL8_CI52,AL:AL,FE;0),,  -100000;   6000   N 09Sun !
  PAR G(FE5AL8_CI52,AL,FE:FE;0),,  -174000;   6000  N 09Sun !
$ Parameters evaluated in the present work
  PAR G(FE5AL8_CI52,TA:AL;0),,  +5*GBCCAL#+8*GHSERTA#; 6000 N 12Wit !
  PAR G(FE5AL8_CI52,TA:FE;0),,  +95000+5*GHSERFE#+8*GHSERTA#;   6000  N 12Wit !
  PAR G(FE5AL8_CI52,AL:TA;0),,  -371750+157*T+8*GBCCAL#+5*GHSERTA#; 6000 N 12Wit !
  PAR G(FE5AL8_CI52,FE:TA;0),,  +95000+8*GHSERFE#+5*GHSERTA#;   6000   N 12Wit !
  PAR G(FE5AL8_CI52,TA:TA;0),,  +65000+13*GHSERTA#; 6000   N 12Wit !

TYPE_DEFINITION ( GES AMEND_PHASE_DESCRIPTION BCC_4SL DIS_PART A2_BCC,,,!
TYPE_DEFINITION ) GES A_P_D BCC_4SL MAGNETIC  -1.0    4.00000E-01 !
 PHASE BCC_4SL:B %()  5 .25   .25   .25   .25   3 !
   CONSTITUENT BCC_4SL:B :AL,FE,TA : AL,FE,TA : AL,FE,TA : VA :  !
  PAR G(BCC_4SL,AL:AL:AL:AL:VA;0),,  +ZERO#;   6000 N 09Sun !
  PAR G(BCC_4SL,AL:AL:AL:FE:VA;0),,  +GD03ALFE#;  6000   N 09Sun !
  PAR TC(BCC_4SL,AL:AL:AL:FE:VA;0),,  -125;   6000  N 09Sun !
  PAR BMAGN(BCC_4SL,AL:AL:AL:FE:VA;0),,  -1.36;    6000   N 09Sun !
  PAR G(BCC_4SL,AL:AL:FE:FE:VA;0),,  +GB2ALFE#;    6000   N 09Sun !
  PAR TC(BCC_4SL,AL:AL:FE:FE:VA;0),,  -250;   6000    N 09Sun !
  PAR BMAGN(BCC_4SL,AL:AL:FE:FE:VA;0),,  -2.72;    6000   N 09Sun !
  PAR G(BCC_4SL,AL:FE:AL:FE:VA;0),,  +GB32ALFE#;   6000   N 09Sun !
  PAR TC(BCC_4SL,AL:FE:AL:FE:VA;0),,  -125;   6000   N 09Sun !
  PAR BMAGN(BCC_4SL,AL:FE:AL:FE:VA;0),,  -1.36;    6000   N 09Sun !
  PAR G(BCC_4SL,AL:FE:FE:FE:VA;0),,  +GD03FEAL#;    6000   N 09Sun !
  PAR TC(BCC_4SL,AL:FE:FE:FE:VA;0),,  -125;   6000   N 09Sun !
  PAR BMAGN(BCC_4SL,AL:FE:FE:FE:VA;0),,  -1.36;    6000   N 09Sun !
  PAR TC(BCC_4SL,AL,FE:*:*:*:VA;0),,  125;   6000    N 09Sun !
  PAR BMAGN(BCC_4SL,AL,FE:*:*:*:VA;0),,  -.3;    6000   N 09Sun !
  PAR BMAGN(BCC_4SL,AL,FE:*:*:*:VA;1),,  -.8;    6000   N 09Sun !
  PAR BMAGN(BCC_4SL,AL,FE:*:*:*:VA;2),,  .2;   6000  N 09Sun !
  PAR G(BCC_4SL,AL,FE:*:*:*:VA;1),,  -634+.68*T;    6000   N 09Sun !
  PAR G(BCC_4SL,AL,FE:*:*:*:VA;2),,  -190;   6000    N 09Sun !
  PAR G(BCC_4SL,AL,FE:AL,FE:*:*:VA;0),,  +ZERO#;    6000   N 09Sun !
  PAR G(BCC_4SL,AL,FE:*:AL,FE:*:VA;0),,  +ZERO#;    6000   N 09Sun !
  PAR G(BCC_4SL,FE:FE:FE:FE:VA;0),,  +ZERO#;   6000  N 09Sun !
```

```
$ Parameters evaluated in the present work
  PAR G(BCC_4SL,TA:TA:TA:TA:VA;0),,  +ZERO#;   6000  N 12Wit !
  PAR G(BCC_4SL,AL:FE:FE:TA:VA;0),,  -ORD1#;   6000   N 12Wit !
  PAR G(BCC_4SL,AL:TA:FE:FE:VA;0),,  -ORD1#;   6000   N 12Wit !
  PAR G(BCC_4SL,AL:FE:TA:TA:VA;0),,  +ORD1#;   6000  N 12Wit !
  PAR G(BCC_4SL,AL:TA:FE:TA:VA;0),,  +ORD1#;   6000  N 12Wit !
  PAR G(BCC_4SL,FE:FE:TA:TA:VA;0),,  +ORD1#;   6000  N 12Wit !
  PAR G(BCC_4SL,FE:TA:FE:TA:VA;0),,  +ORD1#;   6000  N 12Wit !
  PAR G(BCC_4SL,AL:AL:FE:TA:VA;0),,  +ORD1#;   6000  N 12Wit !
  PAR G(BCC_4SL,AL:FE:AL:TA:VA;0),,  +ORD1#;   6000  N 12Wit !
  PAR G(BCC_4SL,AL:AL:TA:TA:VA;0),,  +ORD1#;   6000  N 12Wit !
  PAR G(BCC_4SL,AL:TA:AL:TA:VA;0),,  +ORD1#;   6000  N 12Wit !

 PHASE EPSILON  %  2 .75   .25 !
   CONSTITUENT EPSILON  :AL : AL,FE,TA :  !
  PAR G(EPSILON,AL:AL;0),,  +20000+GHSERAL#;   6000  N 10Wit !
  PAR G(EPSILON,AL:TA;0),,  -29950+6.576*T+.75*GHSERAL#+.25*GHSERTA#; 6000 N 10Wit !
  PAR G(EPSILON,AL:AL,TA;0),,  -1494-10.6211*T;    6000   N 10Wit !
$ Parameters evaluated in the present work
  PAR G(EPSILON,AL:FE,TA;0),,  -15000;   6000   N 12Wit  !
  PAR G(EPSILON,AL:FE;0),,  -2000+.75*GHSERAL#+.25*GHSERFE#; 6000 N 12Wit !

TYPE_DEFINITION * GES AMEND_PHASE_DESCRIPTION FCC_L12 DIS_PART A1_FCC,,,!
TYPE_DEFINITION + GES A_P_D FCC_L12 MAGNETIC  -3.0    2.80000E-01 !
 PHASE FCC_L12:F %*+  5 .25   .25   .25   .25   1 !
   CONSTITUENT FCC_L12:F :AL,FE,TA : AL,FE,TA : AL,FE,TA : AL,FE,TA : VA :  !
  PAR G(FCC_L12,AL:AL:AL:AL:VA;0),,  +ZERO#;   6000   N 09Sun !
  PAR G(FCC_L12,FE:AL:AL:AL:VA;0),,  +GAL3FE#;   6000   N 09Sun  !
  PAR G(FCC_L12,FE:FE:AL:AL:VA;0),,  +GAL2FE2#;  6000  N 09Sun  !
  PAR G(FCC_L12,FE:FE:FE:AL:VA;0),,  +GALFE3#;   6000   N 09Sun  !
  PAR G(FCC_L12,FE:FE:FE:FE:VA;0),,  +ZERO#;   6000      N 09Sun  !
  PAR G(FCC_L12,AL,FE:AL,FE:*:*:VA;0),,  +SFALFE#; 6000 N 09Sun !

 PHASE TA3FE2  %  2 2   3 !
   CONSTITUENT TA3FE2  :AL,FE,TA : AL,FE,TA :  !
  PAR G(TA3FE2,FE:FE;0),,  +5*GHSERFE#+30000;   6000   N 11Wit  !
  PAR G(TA3FE2,TA:FE;0),,  +2*GHSERTA#+3*GHSERFE#+30000;   6000   N 11Wit  !
  PAR G(TA3FE2,FE:TA;0),,  +2*GHSERFE#+3*GHSERTA#+30000;   6000   N 11Wit  !
  PAR G(TA3FE2,TA:TA;0),,  +5*GHSERTA#+80000;   6000   N 11Wit  !
  PAR G(TA3FE2,FE,TA:*;0),,  -60000+10*T;   6000   N 11Wit  !
  PAR G(TA3FE2,*:FE,TA;0),,  -30000+20*T;   6000   N 11Wit  !
$ Parameters evaluated in the present work
  PAR G(TA3FE2,AL:AL;0),,  +5*GHSERAL#+30000;   6000   N 12Wit  !
  PAR G(TA3FE2,FE:AL;0),,  +2*GHSERFE#+3*GHSERAL#+30000;   6000   N 12Wit  !
  PAR G(TA3FE2,TA:AL;0),,  +2*GHSERTA#+3*GHSERAL#+30000;   6000   N 12Wit  !
  PAR G(TA3FE2,AL:FE;0),,  +2*GHSERAL#+3*GHSERFE#+30000;   6000   N 12Wit  !
  PAR G(TA3FE2,AL:TA;0),,  +2*GHSERAL#+3*GHSERTA#+30000;   6000   N 12Wit  !

 PHASE KAPPA  %  2 .6389   .3611 !
   CONSTITUENT KAPPA  :AL,FE,TA : AL,FE,TA :  !
  PAR G(KAPPA,AL:AL;0),,  +GHSERAL#+3000;   6000    N 10Wit !
  PAR G(KAPPA,TA:AL;0),,  +.6389*GHSERTA#+.3611*GHSERAL#; 6000   N 10Wit !
  PAR G(KAPPA,AL:TA;0),,  -25904+3.502*T+.6389*GHSERAL#+.3611*GHSERTA#; 6000 N 10Wit !
  PAR G(KAPPA,TA:TA;0),,  +GHSERTA#+9000;   6000    N  10Wit  !
$ Parameters evaluated in the present work
  PAR G(KAPPA,FE:AL;0),,  +.6389*GHSERFE#+.3611*GHSERAL#; 6000   N  12Wit   !
  PAR G(KAPPA,AL:FE;0),,  +.6389*GHSERAL#+.3611*GHSERFE#; 6000   N  12Wit   !
  PAR G(KAPPA,FE:FE;0),,  +GHSERFE#+9000;   6000   N  12Wit    !
  PAR G(KAPPA,TA:FE;0),,  -4000+.6389*GHSERTA#+.3611*GHSERFE#; 6000 N 12Wit  !
  PAR G(KAPPA,FE:TA;0),,  -4000+.6389*GHSERFE#+.3611*GHSERTA#; 6000 N 12Wit  !
  PAR G(KAPPA,AL,FE:TA;0),,  +58500-42.7*T;   6000  N 12Wit  !

 PHASE LAVES_C14  %  2 2   1 !
   CONSTITUENT LAVES_C14  :AL,FE,TA : AL,FE,TA :  !
  PAR G(LAVES_C14,FE:FE;0),,  +15000+3*GHSERFE#;   6000   N 11Wit  !
  PAR G(LAVES_C14,TA:FE;0),,  +GHSERFE#+2*GHSERTA#;    6000   N 11Wit  !
  PAR G(LAVES_C14,FE:TA;0),,  -36443+.971*T+2*GHSERFE#+GHSERTA#; 6000 N 11Wit !
  PAR G(LAVES_C14,TA:TA;0),,  +18000+3*GHSERTA#;   6000   N 11Wit !
  PAR G(LAVES_C14,FE,TA:FE;0),,  -4166+23.992*T;   6000   N 11Wit !
  PAR G(LAVES_C14,FE:FE,TA;0),,  +28062-8.771*T;   6000   N 11Wit !
  PAR G(LAVES_C14,TA:FE,TA;0),,  +28062-8.771*T;    6000   N 11Wit  !
  PAR G(LAVES_C14,FE,TA:TA;0),,  -12832+28.525*T;   6000   N 11Wit  !
$ Parameters evaluated in the present work
  PAR G(LAVES_C14,AL:AL;0),,  +15000+3*GHSERAL#;    6000   N  12Wit  !
  PAR G(LAVES_C14,FE:AL;0),,  +2*GHSERFE#+GHSERAL#;   6000   N  12Wit   !
  PAR G(LAVES_C14,TA:AL;0),,  +2*GHSERTA#+GHSERAL#;   6000   N  12Wit   !
  PAR G(LAVES_C14,AL:FE;0),,  +GHSERFE#+2*GHSERAL#;   6000   N  12Wit   !
  PAR G(LAVES_C14,AL:TA;0),,  -61000+6.313*T+GHSERTA#+2*GHSERAL#; 6000 N 12Wit !
```

```
  PAR G(LAVES_C14,FE:AL,TA;0),,  -105000;   6000   N  12Wit   !
  PAR G(LAVES_C14,FE:AL,FE,TA;0),,  -537000+277*T;   6000   N 12Wit  !
  PAR G(LAVES_C14,AL:FE,TA;0),,  -219000+115*T;   6000   N 12Wit  !
  PAR G(LAVES_C14,AL,FE:TA;0),,  -115000;   6000   N  12Wit  !
  PAR G(LAVES_C14,AL,FE,TA:TA;0),,  700000;   6000  N  12Wit  !

 PHASE LIQUID  %  1  1.0  !
   CONSTITUENT LIQUID  :AL,FE,TA :  !
  PAR G(LIQUID,AL;0),,  +GLIQAL#;   6000  N  91Din  !
  PAR G(LIQUID,FE;0),,  +GLIQFE#;   6000  N  91Din  !
  PAR G(LIQUID,TA;0),,  +GLIQTA#;   6000  N  91Din  !
  PAR G(LIQUID,AL,FE;0),,  -88090+19.8*T;   6000    N 09Sun !
  PAR G(LIQUID,AL,FE;1),,  -3800+3*T;   6000   N  09Sun !
  PAR G(LIQUID,AL,FE;2),,  -2000;   6000   N  09Sun !
  PAR G(LIQUID,AL,TA;0),,  -55025+9.489*T;   6000   N 10Wit !
  PAR G(LIQUID,AL,TA;1),,  -32750+19.689*T;   6000   N 10Wit !
  PAR G(LIQUID,AL,TA;2),,  +26570-4.667*T;   6000   N 10Wit !
  PAR G(LIQUID,FE,TA;0),,  -34960+7.457*T;   6000    N 11Wit !
  PAR G(LIQUID,FE,TA;1),,  -14992+13.697*T;   6000   N 11Wit !
  PAR G(LIQUID,FE,TA;2),,  +2086-8.942*T;   6000   N 11Wit !
  PAR G(LIQUID,FE,TA;3),,  +8.654*T;   6000   N 11Wit !
$ Parameters evaluated in the present work
  PAR G(LIQUID,AL,FE,TA;0),, -238000+175*T; 6000 N 12Wit !
  PAR G(LIQUID,AL,FE,TA;1),,  +30000-45*T; 6000 N 12Wit !
  PAR G(LIQUID,AL,FE,TA;2),,  +10000-45*T;  6000 N 12Wit  !


 PHASE MU  %  3 7  2  4 !
   CONSTITUENT MU  :AL,FE,TA : TA : AL,FE,TA :  !
  PAR G(MU,FE:TA:FE;0),,  +21500+7*GFCCFE#+4*GHSERFE#+2*GHSERTA#; 6000 N 11Wit !
  PAR G(MU,TA:TA:FE;0),,  +4*GHSERFE#+9*GHSERTA#;   6000   N 11Wit !
  PAR G(MU,FE:TA:TA;0),,  -158214+11.622*T+7*GFCCFE#+6*GHSERTA#;   6000   N  11Wit  !
  PAR G(MU,TA:TA:TA;0),,  +77000+13*GHSERTA#;   6000   N 11Wit !
  PAR G(MU,FE,TA:TA:FE;0),,  -16008+71.487*T;   6000   N 11Wit !
  PAR G(MU,FE,TA:TA:TA;0),,  -16008+71.487*T;   6000   N  11Wit  !
$ Parameters evaluated in the present work
  PAR G(MU,AL:TA:AL;0),,  +11*GHSERAL#+2*GHSERTA#;   6000   N 12Wit !
  PAR G(MU,FE:TA:AL;0),,  +4*GHSERAL#+2*GHSERTA#+7*GHSERFE#;   6000   N 12Wit !
  PAR G(MU,TA:TA:AL;0),,  +2*GHSERAL#+11*GHSERTA#;   6000   N 12Wit !
  PAR G(MU,AL:TA:FE;0),,  +7*GHSERAL#+2*GHSERTA#+4*GHSERFE#;   6000   N 12Wit !
  PAR G(MU,AL:TA:TA;0),,  -247000+18*T+7*GHSERAL#+6*GHSERTA#;   6000   N 12Wit !
  PAR G(MU,AL,FE:TA:TA;0),,  -385000;   6000   N  12Wit !
  PAR G(MU,AL,FE:TA:TA;1),,  -80000;   6000   N  12Wit  !
  PAR G(MU,AL,FE,TA:TA:TA;0),,  200000;   6000   N  12Wit !
  PAR G(MU,AL,FE,TA:TA:TA;1),,  -1250000;   6000   N  12Wit  !
  PAR G(MU,AL,FE,TA:TA:TA;2),,  900000;   6000   N 12Wit !


 PHASE PHI  %  2 .8837   1.1163 !
   CONSTITUENT PHI  :AL,FE,TA : AL,FE,TA :  !
  PAR G(PHI,AL:AL;0),,  +500+2*GHSERAL#;   6000   N 10Wit !
  PAR G(PHI,TA:AL;0),,  +1.1163*GHSERAL#+.8837*GHSERTA#;   6000  N 10Wit !
  PAR G(PHI,AL:TA;0),,  -49300+5.021*T+.8837*GHSERAL#+1.1163*GHSERTA#; 6000 N 10Wit !
  PAR G(PHI,TA:TA;0),,  +22500+2*GHSERTA#;   6000   N 10Wit  !
  PAR G(PHI,AL:AL,TA;0),,  -52500+32.7892*T;   6000 N 10Wit  !
  PAR G(PHI,AL,TA:TA;0),,  -27895.6+8.5005*T;   6000   N 10Wit  !
$ Parameters evaluated in the present work
  PAR G(PHI,FE:AL;0),,  +.8837*GHSERFE#+1.1163*GHSERAL#; 6000 N 12Wit !
  PAR G(PHI,AL:FE;0),,  -10000+.8837*GHSERAL#+1.1163*GHSERFE#;   6000   N 12Wit !
  PAR G(PHI,FE:FE;0),,  +10000+2*GHSERFE#;   6000   N  12Wit  !
  PAR G(PHI,TA:FE;0),,  +10000+.8837*GHSERTA#+1.1163*GHSERFE#;   6000   N 12Wit !
  PAR G(PHI,FE:TA;0),,  +10000+.8837*GHSERFE#+1.1163*GHSERTA#;   6000   N 12Wit !

 PHASE SIGMA  %  3 .533   .333   .134 !
   CONSTITUENT SIGMA  :AL,FE,TA : AL,FE,TA : TA :  !
  PAR G(SIGMA,AL:AL:TA;0),,  -11403+7.0992*T+.866*GHSERAL#+.134*GHSERTA#;   6000  N 10Wit !
  PAR G(SIGMA,TA:AL:TA;0),,  +.667*GHSERTA#+.333*GHSERAL#-22048+3.0651*T;   6000  N 10Wit !
  PAR G(SIGMA,AL:TA:TA;0),,  +.533*GHSERAL#+.467*GHSERTA#; 6000   N 10Wit  !
  PAR G(SIGMA,TA:TA:TA;0),,  +2.4499*T+GHSERTA#;   6000   N 10Wit !
  PAR G(SIGMA,AL,TA:AL:TA;0),,  -22068.5;   6000   N 10Wit !
$ Parameters evaluated in the present work
  PAR G(SIGMA,FE:AL:TA;0),,  +.533*GHSERFE#+.333*GHSERAL#+.134*GHSERTA#; 6000  N 12Wit !
  PAR G(SIGMA,AL:FE:TA;0),,  +.533*GHSERAL#+.333*GHSERFE#+.134*GHSERTA#; 6000  N 12Wit !
```

```
   PAR G(SIGMA,FE:FE:TA;0),,  +4000+.866*GHSERFE#+.134*GHSERTA#;   6000   N 12Wit !
   PAR G(SIGMA,TA:FE:TA;0),,  +4000+.667*GHSERTA#+.333*GHSERFE#;   6000   N 12Wit !
   PAR G(SIGMA,FE:TA:TA;0),,  +4000+.533*GHSERFE#+.467*GHSERTA#;   6000   N 12Wit !
   PAR G(SIGMA,TA:AL,FE:TA;0),,  -15000;   6000   N 12Wit !
   PAR G(SIGMA,TA:AL,FE,TA:TA;0),,  -35000;   6000   N 12Wit !
   PAR G(SIGMA,TA:AL,FE,TA:TA;1),,  -50000;   6000   N 12Wit !
   PAR G(SIGMA,TA:AL,FE,TA:TA;2),,  -110000;   6000  N 12Wit !

ASSESSED_SYSTEM AL-FE(G5 C_S:BCC_4/AL:AL:FE:FE:VA:
 C_S:BCC_4/AL:FE:FE:FE:VA: ;P3 TMM:300/3000 STP:0.99/1400/-1 STP:0.77/600/1 STP:0.45/500/1 )
 AL-TA(P3 TMM:300/3000 STP:0.5/1500/1) FE-TA(P3 TMM:300/3000 STP:0.5/1500/1)
 AL-FE-TA(G5 C_S:BCC_4/AL:AL:FE:FE:VA: C_S:BCC_4/AL:FE:FE:FE:VA:
 ;P3 TMM:300/3000 STP:0.99/1400/-1 STP:0.77/600/1 STP:0.45/500/1 ) !

LIST-OF-REFERENCE
 NUMBER  SOURCE
         SSUB4  'SGTE Substances Database, Version 4.1, Aug. 2008'
         91Din    'A.T. Dinsdale, Calphad, 15, 317-425(1991)'
         09Sun    'B. Sundman et al., Acta Mater, 57, 2896-2908 (2009)'
         10Wit    'V.T. Witusiewicz et al., Intermetallics 18, 92-106 (2010)'
         11Wit    'V.T. Witusiewicz et al., Intermetallics 19, 1059-1075 (2011)'
         12Wit    'Present work'
```

References

1. Sauthoff G (2000) Intermetallics 8:1101
2. Hanus P, Bartsch E, Palm M, Krein R, Bauer-Partenheimer K, Janschek P (2010) Intermetallics 18:1379
3. Risanti DD, Sauthoff G (2005) Mat Sci Forum 475–479:865
4. Hotař A, Palm M (2010) Intermetallics 18:1390
5. Yoshimi K, Hanada S (1997) JOM 49:46
6. Reviere R, Sauthoff G, Johnson DR, Oliver BF (1997) Intermetallics 5:161
7. Risanti DD, Sauthoff G (2005) Intermetallics 13:1313
8. Palm M (2009) Fe-Al materials for structural applications at high temperatures: current research at MPIE. Int J Mat Res 100: 277–287
9. Palm M, Krein R, Milenkovic S, Sauthoff G, Risanti D, Stallybrass C, Schneider A (2007) Mat Res Soc Symp Proc 980:II01
10. Kaufman L (1991) Calphad 15:261
11. Sundman B, Ohnuma I, Dupin N, Kattner UR, Fries SG (2009) Acta Mater 57:2896
12. Witusiewicz VT, Bondar AA, Hecht U, Zollinger J, Petyukh VM, Fomichov OS, Voblikov VM (2010) Intermetallics 18:92
13. Witusiewicz VT, Bondar AA, Hecht U, Voblikov VM, Fomichov OS, Petyukh VM, Rex S (2011) Intermetallics 19:1059
14. Ghosh G (2008) In: Effenberg G, Ilyenko S (eds) Landolt–Börnstein, numerical data and functional relationships in science and technology, (New Series) Group IV: Martinsen W (ed) Physical chemistry, ternary alloy systems. Phase diagrams, crystallographic and thermodynamic data critically evaluated by MSIT, Vol. 11D1. Springer, Berlin, p 213
15. Kumar KS (1990) Int Mater Rev 35:293
16. Raghavan V (1992) In: Phase diagrams of ternary iron alloys, Part 6A. Indian Institute of Metals, Calcutta, p 187
17. Ghosh G (1992) In: Petzov G, Effenberg G (eds), Ternary alloys: a comprehensive compendium of evaluated constitutional data and phase diagrams, Vol. 5. VCH Verlaggeselschaft mbH, Weinheim, p 449
18. Tsai AP, Inoue A, Masumoto T (1988) Jpn J Appl Phys 27:L5
19. Srinivas V, McHenry ME, Dunlap RA (1989) Phys Rev 40B:9590
20. Hunt CR, Raman A (1968) Z Metallkde 59:701
21. Von Keitz A, Sauthoff G, Neumann P (1998) Z Metallkde 89:803
22. Risanti DD, Sauthoff G (2006) Entwicklung ferritischer Eisen-Aluminium-Tantal-Legierungen mit verstärkender Laves-Phase mit höchster Zeitstandfestigkeit in korrosiven Atmosphären. DFG Abschlussbericht
23. Risanti DD (2010) Development of ferritic Fe–Al–Ta alloys with strengthening Laves phase for high temperature applications. Dissertation. RWTH Aachen
24. Risanti DD, Sauthoff G (2011) Intermetallics 19:1727
25. Anthony L, Fultz B (1995) Acta Metall Mater 43:3885
26. Bozzolo GH, Noebe RD, Amador C (2002) Intermetallics 10:149
27. Mekhrabov AO, Akdeniz MV (1999) Acta Mater 47:2067
28. Drevermann A, Pickmann C, Tiefers R, Zimmermann G (2004) Ultrasonics 42:105
29. Schneider A, Falat L, Sauthoff G, Frommeyer G (2003) Intermetallics 11:443
30. Kocherzhinsky JuA (1971) Proc Third ICTA (Davos) 1:549
31. Kocherzhinsky JuA, Shishkin YeA, Vasilenko VI (1971) Apparatus for differential thermal analysis with temperature-sensing thermocouple up to 2200 °C. In: Ageev NV, Ivanov OS (eds) Nauka, Moskow, pp 245-249 (in Russian)
32. Boettinger WJ, Kattner UR, Moon K-W, Perepezko JH (2006) DTA and heat-flux DSC measurements of alloy melting and freezing, NIST recommended practice guide. NIST, Special publication 960-15
33. Witusiewicz VT, Sommer F, Mittemeijer EJ (2003) Met Mater Trans 34B:209
34. Witusiewicz VT, Fries SC, Hecht U, Drevermann A, Rex S (2006) Int J Mater Res 97:556
35. Dinsdale AT (1991) SGTE data for pure elements. Calphad 15:317
36. PURE4 SGTE database. http://www.thermocalc.se/Products/Databases.html; http://www.thermocalc.com/res/Manuals/tc_database_guide.pdf
37. Sundman B, Jansson B, Andersson J-O (1985) Calphad 9:153
38. Lukas HL, Fries SG, Sundman B (2007) Computational thermodynamics. Cambridge Univ. Press, Cambridge
39. Ohnuma I, Schön CG, Kainuma R, Inden G, Ishida K (1998) Acta Mater 46:2083
40. Witusiewicz VT, Bondar AA, Hecht U, Velikanova TY (2011) J Phase Equ Diff 32:329
41. Bean CP, Rodbell DS (1962) Phys Rev 126:104
42. Stout JW (1948) Phys Rev 74:605
43. Laughlin DE, Srinivasan K, Tanase M, Wang L (2005) Scripta Mat 53:383
44. Allen SM, Cahn JW (1982) Bull Alloy Phase Diagr 3:287

45. Inden G (1982) Bull Alloy Phase Diagr 2:412
46. Chang YA (1989) Bull Alloy Phase Diagr 10:513
47. Talanquer V, Varea C, Robledo A (1989) Phys Rev B 39:7030
48. Matsumura S (1998) Z Metallkde 89:814
49. Lukas HL, Henig E-T, Petzow G (1986) Z Metallkde 77:360
50. Palm M, Lacaze J (2006) Intermetallics 14:1291
51. Dovbenko O, Stein F, Palm M, Prymak O (2010) Intermetallics 18:2191
52. Prymak O, Stein F (2010) Intermetallics 18:1322